Nanoscale

ROYAL SOCIETY OF CHEMISTRY

REVIEW

View Article Online
View Journal | View Issue

Cite this: *Nanoscale*, 2024, **16**, 10087

Recent progress in atomically precise silver nanocluster-assembled materials

Noohul Alam,† Anish Kumar Das, † Priyanka Chandrashekar, Priyadarshini Baidya and Sukhendu Mandal *

In the dynamic landscape of nanotechnology, atomically precise silver nanoclusters (Ag NCs) have emerged as a novel and promising category of materials with their fascinating properties and enormous potential. However, recent research endeavors have surged towards stabilizing Ag-based NCs, leading to innovative strategies like connecting cluster nodes with organic linkers to construct hierarchical structures, thus forming Ag-based cluster-assembled materials (CAMs). This approach not only enhances structural stability, but also unveils unprecedented opportunities for CAMs, overcoming the limitations of individual Ag NCs. In this context, this review delves into the captivating realm of atomically precise nitrogen-based ligand bonded Ag(I)-based CAMs, providing insights into synthetic strategies, structure–property relationships, and diverse applications. We navigate the challenges and advancements in integrating Ag(I) cluster nodes, bound by argentophilic interactions, into highly connected periodic frameworks with different dimensionalities using nitrogen-based linkers. Despite the inherent diversity among cluster nodes, Ag(I) CAMs demonstrate promising potential in sensing, catalysis, bio-imaging, and device fabrication, which all are discussed in this review. Therefore, gaining insight into the silver nanocluster assembly process will offer valuable information, which can enlighten the readers on the design and advancement of Ag(I) CAMs for state-of-the-art applications.

Received 31st March 2024,
Accepted 23rd April 2024

DOI: 10.1039/d4nr01411a

rsc.li/nanoscale

1. Introduction

In a 1959 address, Feynman envisioned 'There's Plenty of Room at the Bottom', foreseeing the ability to assemble materials at the atomic level.[1] Although initially overlooked by the research community, it gained recognition in the 1980s when researchers referenced it to establish scientific credibility in what we now know as nanotechnology. Feynman's contemplation of manipulating matter at the atomic scale laid the groundwork for the field. Consequently, the realm of nanoscale materials has flourished, spanning sizes from 1 to 100 nm.[2,3] In recent years, metal nanoclusters with precise atomic arrangements, typically sized below 3 nm, have

School of Chemistry, Indian Institute of Science Education and Research Thiruvananthapuram, Thiruvananthapuram, Kerala, India 695551.
E-mail: sukhendu@iisertvm.ac.in
† These authors contributed equally to this work.

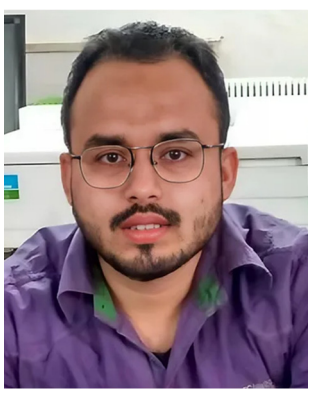

Noohul Alam

Noohul Alam received his PhD degree from the Indian Institute of Technology Patna, India. Currently, he is working as a postdoctoral fellow at the Indian Institute of Science Education and Research Thiruvananthapuram, India. His research focuses on functional silver and copper nanoclusters and their assembly.

Anish Kumar Das

Anish Kumar Das received his Ph.D. degree in chemistry from the Indian Institute of Science Education and Research Thiruvananthapuram, India. Currently, he is working as a postdoctoral fellow at the University of Illinois Urbana-Champaign, USA. He works on functional molecular and nanoscale materials.

emerged as a novel category of nanomaterials exhibiting distinctive characteristics.[4–9] Significant attention has been devoted to investigating their synthesis methods, molecular compositions, structural intricacies, and inherent properties, along with exploring their potential applications.[5,10–14] These atomically precise metal nanoclusters (NCs) demonstrate traits akin to molecules, such as chirality, HOMO–LUMO transitions, catalytic activity, luminescence, *etc*. Notably, these properties are intricately linked to the size, composition, and structure of NCs.[15–24] Even slight alterations in their formula or structure can lead to substantial variations in their properties, underscoring the imperative for precise control during their synthesis.[25–28]

Among the various types of NCs, gold (Au) and silver (Ag) hold particular significance with numerous sizes and structures.[29–31] While extensive research has been conducted on Au NCs, the exploration of Ag NCs remains comparatively limited.[32–34] Despite their similar atomic radius (2.89 Å for Ag and 2.88 Å for Au) owing to their placement in the same group 11, Ag exhibits greater reactivity and susceptibility to oxidation compared to Au.[34,35] Therefore, the properties of silver NCs mostly depend upon the oxidation state (*i.e.* mixed valence $Ag^{+/0}$ or Ag^{+}) of the core architecture of Ag-based NCs.[36,37] While there have been strides in synthesizing NCs containing mixed valence Ag atoms, the exploration of Ag(I)-based NCs has only recently commenced, aiming to address stability concerns.[38] In the case of Ag(I) NCs, the cluster node is made up of Ag(I)···Ag(I) argentophilic interactions instead of the usual metallic bonding due to the unavailability of valence electrons in the silver atoms.[39–41] This unique bonding makes them inherently unstable because argentophilic interactions are prone to oxidation and external factors such as pH, heat, light changes, and the presence of guest molecules, presenting challenges in the synthesis and crystal structure determination of Ag(I) NCs.[34,42] Furthermore, it also restricts their potential applications across various fields. Drawing inspiration from the reticular construction of metal–organic frameworks (MOFs), there has been growing interest in assembling Ag(I) NCs into atomically precise cluster-based assembled materials (CAMs) with the incorporation of organic linkers to address these limitations.[43–45] CAMs offer a combined benefit of MOFs and NCs, such as highly connected frameworks with robust structures, extensive structural tunability, and high-nuclearity cluster nodes.[44] The employment of Ag(I) cluster nodes as fundamental building blocks alongside nitrogen-based linker molecules has increasingly led to the development of a plethora of arrangements such as one-dimensional (1D), two-dimensional (2D), and three-dimensional (3D) Ag(I) CAMs (Fig. 1).[46–48] Although the integration of discrete cluster nodes exhibits challenges due to the influence of the chemical properties of individual cluster nodes, which vary based on the number of atoms present at the nodes.[49–51] Mak and colleagues have spearheaded significant advancements in the synthesis and structural elucidation of multidimensional Ag NC-based materials, showcasing a profound understanding of their intricate architectures.[52,53] Similarly, Sun and collaborators have made substantial strides, unveiling a series of multidimensional self-assembled clusters. Their innovative use of polyoxometallates as an anionic template, coupled with organic ligands and halide atoms as linkers, has enabled the creation of intricate and functional CAMs with tailored properties.[54,55] Zhu and team have also left an indelible mark on the field, synthesizing remarkable 3D structures composed of $[Au_1Ag_{22}(AdmS)_{12}](SbF_6)_2Cl$ and $[Au_1Ag_{22}(AdmS)_{12}](SbF_6)_3$ as fundamental structural units.[56] These CAM materials have emerged as highly efficient fluorescence probes, capitalizing on their unique fluorescence properties to detect organic compounds with unprecedented sensitivity and selectivity. The enhanced stability of CAMs is due to the formation of rigid coordination framework structures.[45] The commonly observed CAMs are empty cuboctahedron Ag_{12} cluster nodes with bi/multidentate linkers.[43] The integration of the properties of cluster nodes and linkers in CAMs shows high emission efficiency, thereby modulating the relative energy level of the cluster core and linker components.[57] Emission in CAMs is usually assigned to the cluster-centered triplet excited state (^{3}CC), n–π* and/or π–π* transition excited state of the protecting ligands, ligand-to-metal–metal charge transfer (LMMCT;

Priyanka Chandrashekar

Priyanka Chandrashekar received her MSc degree in chemistry from Bangalore University, Bengaluru, India. She is currently pursuing her PhD at the Indian Institute of Science Education and Research, Thiruvananthapuram, India. Her research centers on synthesizing and analyzing the structure–property correlation in multidimensional silver nanocluster-assembled materials.

Priyadarshini Baidya

Priyadarshini Baidya is in her final year of BS-MS dual degree at the Indian Institute of Science Education and Research, Thiruvananthapuram, majoring in chemistry with biology as a minor subject. She is pursuing her master's thesis under the supervision of Prof. Sukhendu Mandal. Her research interests span over noble metal cluster assemblies, tuning their structure-dependent properties.

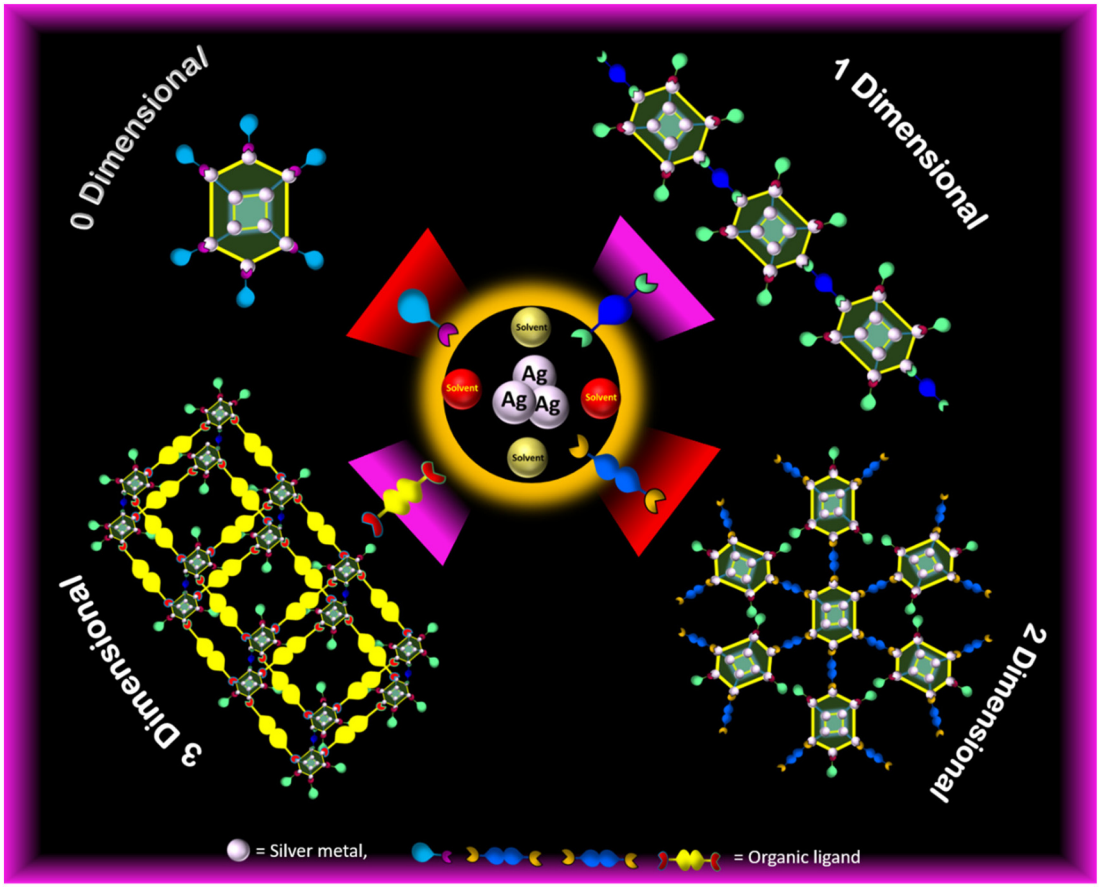

Fig. 1 Schematic illustration of different arrangements of Ag(I) CAMs, such as one-dimensional (1D), two-dimensional (2D), and three-dimensional (3D) framework structures.

S → Ag), and interligand trans-metallic charge transfer transition (ITCT, S/Ag → Py).[37] CAMs allow the feasibility of multi emission centers which can be further modulated/tuned by the cluster arrangement/linker/temperature.[58–60] Lowering the temperature significantly enhances the emission intensity with a microsecond lifetime, and emission is usually found to be red-shifted. The former could be due to the rigidity and heavy atom effect-induced intersystem crossing, while the latter is due to the contraction of Ag···Ag interactions which influences the energy level related to the ^{3}CC state, thus lowering the energy level of the cluster centered state.[60] These characteristics of CAMs along with their specific size, geometry, and ease of handling act as functional nanomaterials for use in nanotechnology which can be put forward for practical applications in the field of sensors, catalysts, photo-harvesting, optical–electrical technology, antibacterial, time-gated imaging, field-effect transistors and so on (Fig. 2).[6,8,42,49,55,57,61–65] Therefore, CAMs become the spotlight in the family of atomically precise NCs, thus fueling the burgeoning landscape of Ag(I) CAM research.

In this context, this review article delves into the fascinating realm of atomically precise nitrogen-based linker-induced Ag(I) CAMs. We begin by exploring various synthetic strategies employed to synthesize these Ag(I) CAMs. We further elucidated the structure–property relationship, shedding light on how the organic linker and solvents influence the atomic arrangement and overall properties of Ag(I) CAMs. We have also paid special attention to the discussion of their potential applications, spanning from sensing to bio-imaging, device

Sukhendu Mandal

Sukhendu Mandal received his Ph.D. from the Indian Institute of Science, Bangalore, India. He then pursued a postdoctoral fellowship at Pennsylvania State University, USA. Currently, he is a professor in chemistry at the Indian Institute of Science Education and Research Thiruvananthapuram, India. He works on functional molecular and nanoscale materials.

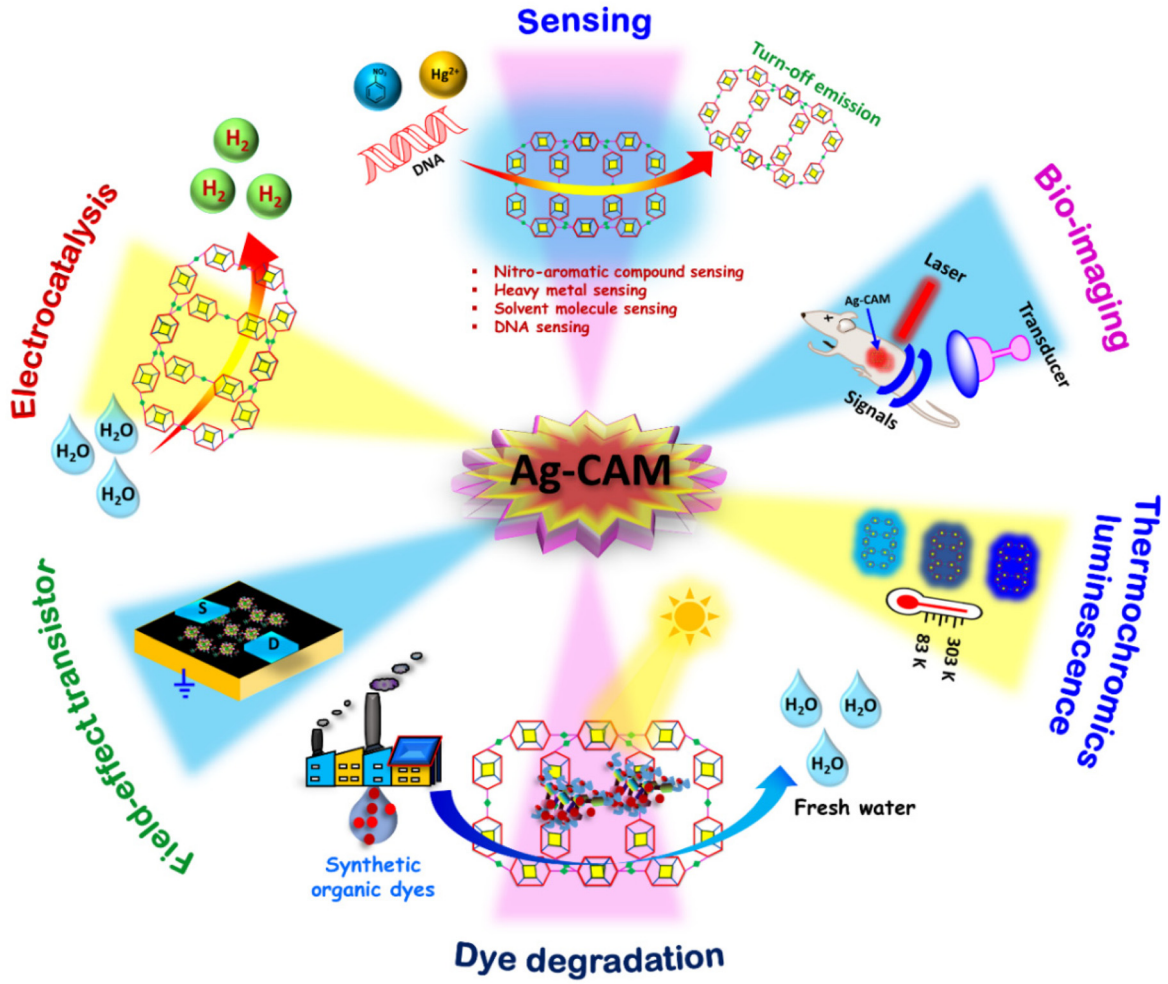

Fig. 2 Schematic illustration of the several applications of Ag(I) CAMs.

fabrication, and catalysis, underscoring their versatility and significance across different fields. To aid readers in grasping the breadth of research in this domain, we present a detailed summary (Table 1) encompassing the essential parameters such as unit-cell dimensions, space group, dimensionality, and notable applications of Ag(I) CAMs reported in the literature. Finally, we contemplate the prospects of Ag(I) CAMs, offering insights into potential advancements and promising possibilities for further exploration and innovation.

2. Synthetic strategy of Ag(I) CAMs

To bolster the stability of individual atom-precise Ag NCs, a pioneering concept emerges wherein cluster nodes intertwine with bidentate or multidentate organic linker molecules, giving rise to an intricate framework architecture.[67] This inventive approach results in Ag(I) CAMs endowed with a variety of intriguing properties, manipulated by the interplay of cluster node geometry, electronic effects of linker molecules, and the overall dimensionality of the materials. To reveal the features, the initial challenge lies in devising a synthetic strategy for CAMs. Traditionally, these materials undergo a two-step synthesis process—initially, the synthesis of precursor complexes, followed by the subsequent addition of metal salts and linker molecules in a specific solvent mixture.[61] This process culminates in the crystallization of CAMs after a certain duration. Understanding the structure becomes important to comprehend the fundamental properties of CAMs.

The synthesis of Ag CAMs indeed yields a significant improvement in stability when compared to individual Ag NCs. This enhancement is exemplified by the transformation of $[(Ag_{12}(S^tBu)_6(CF_3COO)_6(CH_3CN)_6)]\cdot CH_3CN$ NCs into a framework-based architecture using a rigid bidentate linker BPY.[45] Through this conversion process, the terminal CH_3CN ligands of the Ag ions are replaced and Ag–S cluster-based nodes are linked by BPY bridges to create a porous coordination framework. This strategic substitution of labile solvent molecules with a nitrogen-based linker leads to a remarkable increase in stability, from mere minutes to years, even under ambient conditions. Similar strategies were observed in the case of enhancing the stability of $[Ag_{14}(C_2B_{10}H_{10}S_2)_6(CH_3CN)_8]\cdot 4CH_3CN$ by

Table 1 List of Ag(I) CAMs with dimensionality, space group, unit cell parameters, and applications

Sl. no.	Formula of Ag(I) CAM node	Linker	Dimensionality	Space group	Unit cell parameters		Application/outcome of the study	Ref.
					(a, b, c) Å	(α, β, γ)°		
1	$[Ag_{10}(S^tBu)_6(CF_3CF_2COO)_4(CH_3CN)_2]$	BPY	1 D	$P\bar{1}$	a = 11.5122(2) b = 13.8084(2) c = 13.9132(2)	α = 2.1340(10) β = 3.8870(10) γ = 82.8960(10)	Solvent sensing	66
2	$[Cl@Ag_{15}(S^tBu)_8(CF_3COO)_{5.67}(NO_3)_{0.33}(DMF)_2]$		1 D	$P\bar{1}$	a = 15.009(2) b = 19.593(3) c = 22.379(3)	α = 96.761(4) β = 101.558(4) γ = 98.432(4)	The anion template (Cl^-) is found to play a crucial role in the formation of the nano-cluster's nuclearity.	44
3	$[Ag_{10}\{S_2P(O^iPr)_2\}_8]$		1 D	$P\bar{1}$	a = 15.9584(6) b = 26.4546(11) c = 27.7795(10)	α = 4.9002(15) β = 77.939(17) γ = 83.565(19)	The study highlights the influence of solvent polarity on optical behavior.	67
4	$[Ag_{10}(S^tBu)_6(CF_3COO)_2(PhPO_3H)_2]$		2 D	$P\bar{1}$	a = 12.1375(6) b = 14.2801(5) c = 17.8065(8)	α = 62.077(2) β = 88.228(2) γ = 79.945(2)	Solvent sensing	46
5	$[Ag_{12}(S^tBu)_6(CF_3COO)_6\cdot(DMAC_x\cdot toluene_y)]$		2 D	$P\bar{3}$	a = 19.2794(3) b = 19.2794(3) c = 11.22041(18)	α = 90 β = 90 γ = 120	The core size of the cluster was found to be very effective in fine-tuning the hypergolic performance.	57
6	$[Cl@Ag_{14}(S^tBu)_8(CF_3COO)_5(DMF)]\cdot 2(DMF)$		2 D	$P\bar{1}$	a = 14.871(1) b = 15.265(1) c = 31.209(3)	α = 76.925(2) β = 88.638(2) γ = 61.957(2)	The anion template (Cl^-) is found to play a crucial role in the formation of the nano-cluster's nuclearity.	44
7	$[Ag_{12}S_2(S^tBu)_8(CF_3COO)_4]$		3 D	$I222$	a = 17.3070(9) b = 17.3297(9) c = 20.7178(10)	α = 90 β = 90 γ = 90	Sensor for nitroaromatic materials	68
8	$[Ag_{12}(S^tBu)_8(CF_3COO)_4]$		3 D	$I\bar{4}2m$	a = 17.34149(13) b = 17.34149(13) c = 20.1671(4)	α = 90 β = 90 γ = 90	Oxygen sensing	45
9	$[Cd_6Ag(SPh)_{16}(DMF)(H_2O)]$	BPE	1 D	$P2_1/n$	a = 18.6194(5) b = 35.7094(11) c = 19.7050(8)	α = 90 β = 92.632(3) γ = 90	Photocatalyst for organic dye degradation	69
10	$[Ag_{12}(S^tBu)_6(CF_3COO)_6(DMAC)_{14.7}]$		2 D	$P\bar{3}$	a = 21.4897(8) b = 21.4897(8) c = 11.2055(5)	α = 90 β = 90 γ = 120	Flexible linker drives cluster transformations	49
11	$[Cd_6Ag_4(SPh)_{16}]$		3 D	$I4_1/a$	a = 18.3203(2) b = 18.3203(2) c = 45.4431(11)	α = 90 β = 90 γ = 120	Photocatalyst for organic dye degradation	70
12	$[Mo_6O_{19}@Ag_{44}(SEt)_{24}(SC_{14})_3]$		3 D	$Fm\bar{3}c$	a = 32.558(4) b = 32.558(4) c = 32.558(4)	α = 90 β = 90 γ = 90	POM template self-assembles core–shell silver cluster structures into higher dimensional materials.	54
13	$[SO_4@Ag_{22}(S^iPr)_{12}(NO_3)_6\cdot 2NO_3]$		3 D	$Fd\bar{3}c$	a = 31.6177(14) b = 31.6177(14) c = 31.6177(14)	α = 90 β = 90 γ = 90	"Large cluster and small bridge" strategy used for the synthesis of silver cluster-based framework materials.	71

Table 1 *(Contd.)*

Sl. no.	Formula of Ag(I) CAM node	Linker	Dimensionality	Space group	Unit cell parameters		Application/outcome of the study	Ref.
					(a, b, c) Å	(α, β, γ)°		
14	$[Ag_{11}(SC_{10}H_{15})_6(CF_3COO)_4(DMF)_2][NO_3]$	AZBPY	1 D	$C2/c$	a = 28.707(5) b = 16.532(3) c = 24.577(4)	α = 90 β = 96.424 γ = 90	Exhibit solvent-dependent photophysical properties	47
15	$[CO_3@Ag_{20}(S^tBu)_{10}(CH_3COO)_8(DMF)_2]$		1 D	$P\bar{1}$	a = 12.947(5) b = 15.169(5) c = 15.922(5)	α = 67.605(5) β = 82.355(5) γ = 65.089(5)	Thermochromic luminescence	72
16	$[V_{10}O_{28}@Ag_{44}(SEt)_{20}(PhSO_3)_{18}(H_2O)_2]$		1 D	$P\bar{1}$	a = 19.9658(6) b = 20.2722(14) c = 20.4027(12)	α = 60.809(7) β = 70.785(4) γ = 78.996(4)	Used to fabricate working electrodes for electrochemical analysis	54
17	$[[HN(CH_3)_2CO]\cdot[CO_3@Ag_{18}(S^tBu)_{10}(NO_3)_7(DMF)_4]\cdot DMF]$		1 D	$P2_1/n$	a = 13.8969(9) b = 14.1770(10) c = 24.1230(17)	α = 90 β = 97.1240(10) γ = 90	Cluster-assembled material was synthesized from a silver carbide precursor Ag_2C_2 using C_2^{2-} a pre-templated approach.	73
18	$[Ag_{12}(S^tBu)_6(CF_3COO)_6]$		2 D	$P\bar{3}m1$	a = 21.085(4) b = 21.085(4) c = 11.032(2)	α = 90 β = 90 γ = 120	Field-effect transistor	62
19	$[Ag_{14}(S^tBu)_{10}(CF_3COO)_4]$		2 D	$C2/c$	a = 23.087(3) b = 14.5454(17) c = 30.330(4)	α = 90 β = 102.868 γ = 90	Photoacoustic imaging	65
20	$[PhPO_3@Ag_{18}(S^tBu)_{10}(CF_3COO)_2(PhPO_3H)_4]$	BPY-NH_2	1 D	$P2_1/n$	a = 18.2031(9) b = 34.9936(10) c = 24.1277(8)	α = 90 β = 94.379 γ = 90	Thermochromic luminescence	74
21	$[Ag_{12}(S^tBu)_8(CF_3COO)_4]$		2 D	$I\bar{4}2m$	a = 17.31644(12) b = 17.31644(12) c = 19.4319(4)	α = 90 β = 90 γ = 90	Oxygen sensing	75
22	$[Ag_{12}(S^tBu)_6(CF_3COO)_6]$	TPPE	3 D	$Pm\bar{3}m$	a = 42.0867(3) b = 42.0867(3) c = 42.0867(3)	α = 90 β = 90 γ = 90	Mesoporous cluster-assembled material exhibits tailorable photoluminescence properties.	58
23	$[Ag_{12}(S^tBu)_6(CF_3COO)_6]_{0.5}[Ag_8(S^tBu)_4(CF_3CO_2)_4]$		3 D	$P\bar{1}$	a = 17.5965(2) b = 26.2516(4) c = 26.9520(4)	α = 60.910(2) β = 80.8650(10) γ = 89.9000(10)	Guest-triggered aggregation-induced emission	48
24	$[Ag_{12}(C_6H_{11}S)_6(CF_3COO)_6(TmPyPB)_2]\cdot(C_4H_8O_2)_3$	TmPyPB	2 D	$P2_1/n$	a = 18.0384(3) b = 23.5623(3) c = 19.6521(3)	α = 90 β = 90.786(2) γ = 90	Cluster packing-dependent emission	59
25	$[Ag_{14}(S^tBu)_{10}(CF_3COO)_4]$	BPA	2 D	$C2/c$	a = 23.2587(6) b = 14.7272(4) c = 30.0370(8)	α = 90, β=102.526(10) γ = 90	DNA detection	76
26	$[Ag_{12}(S^tBu)_6(CF_3COO)_6]$	BPEB	2 D	$R\bar{3}m$	a = 28.808(2) b = 28.808(2) c = 11.3966(14)	α = 90 β = 90 γ = 90		76
27	$[CO_3@Ag_{20}(S^iPr)_{10}(NO_3)_8(DMF)_2]$		2 D	$P\bar{1}$	a = 12.9823(9) b = 13.0556(9) c = 14.1121(8)	α = 86.907(6) β = 71.281(5) γ = 68.890(5)	"Large cluster and small bridge" strategy used for the synthesis of silver cluster-based framework materials	71
28	R-$[Cl@Ag_{17}(S^iPr)_9S(CH_3COO)_5H_2O]$		2 D	$P2_12_12_1$	a = 14.604(2) b = 22.079(3) c = 22.458(3)	α = 90 β = 90 γ = 90	Catalyst for H_2O splitting	8
29	S-$[Cl@Ag_{17}(S^iPr)_9S(CH_3COO)_5H_2O]$				a = 14.5977(9) b = 22.0096(13) c = 22.4902(14)	α = 90 β = 90 γ = 90		
30	$Ag_{46}(V_{10}O_{28})(SEt)_{23}(PhSO_3)_{15}(CO_3)$		2 D	Cm	a = 25.7510(15) b = 30.6808(17) c = 19.5302(11)	α = 90, β = 126.5766(6) γ = 90	POMs template the self-assembly of core–shell silver cluster structures into higher dimensional materials	54

Table 1 *(Contd.)*

Sl. no.	Formula of Ag(I) CAM node	Linker	Dimensionality	Space group	Unit cell parameters		Application/outcome of the study	Ref.
					(a, b, c) Å	(α, β, γ)°		
31	$[Ag_{27}S_2(S^tBu)_{14}(CF_3COO)_8](CF_3COO)$	TPyP	2 D	*Cmcm*	a = 24.2026(5), b = 21.3506(6), c = 37.2253(10)	α = 90 β = 90 γ = 90	Catalyst for CO_2 fixation	55
32	$[Ag_{12}(S^tBu)_6(CF_3COO)_3]$		2 D	$P\bar{1}$	a = 14.77100(10) b = 15.4918(2) c = 15.6410(2)	α = 61.4520 (10) β = 68.2290(10) γ = 67.3880(10)	Excellent photocatalyst for selective oxidation of a mustard simulant	77
33	$[Ag_9(^tBuC{=}C)_6(CF_3COO)_3]$	Ag-TPyP	2 D	*C*2/*c*	a = 24.5697(8) b = 19.2501(5) c = 22.6181(6)	α = 90 β = 98.112(3) γ = 90	Bioprotective material against superbacteria	78
34	$[Ag_{10}(S^tBu)_6(CF_3COO)_4(CH_3CN)]$	2-PCH	1 D	$P2_1/c$	a = 12.6074(12) b = 27.316(3) c = 25.206(3)	α = 90 β = 101.714(3) γ = 90	Sensor for dichloromethane or trichloromethane in tetrachloromethane	79
35	$[Ag_{10}(S^tBu)_6(CF_3COO)_4(CH_3CN)_4]$	3-PCH	2 D	$P2_1/n$	a = 15.8445(14) b = 16.3701(14) c = 17.0804(15)	α = 90 β = 111.842(2) γ = 90	Space distribution of the coordination site plays a crucial role in controlling the dimensionality of the material	79
36	$[Ag_{10}(S^tBu)_6(CF_3COO)_4(CH_3CN)_2]$	4-PCH	1 D	*C*2/*c*	a = 27.055(3) b = 16.7198(19) c = 18.698(2)	α = 90 β = 94.502(2) γ = 90		79
37	$[Ag_{12}(S^tBu)_6(CF_3COO)_6]$	TPBTC	3 D	$R\bar{3}$	a = 24.1539(5) b = 24.1539(5) c = 20.9231(9)	α = 90 β = 90 γ = 120	Catalyst for hexacyanoferrate(III) reduction	80
38	$[Ag_{12}(S^tBu)_6(CF_3COO)_6(DMAC)_{14.7}]$	BPA	2 D	$P\bar{3}$	a = 21.4789(4) b = 21.4789(4) c = 11.2991(3)	α = 90 β = 90 γ = 120	Flexible linker drives cluster transformations	49
39	$[Ag_{12}S_2(S^tBu)_8(CF_3COO)_4]$	Pyrazine	2 D	$P\bar{3}m1$	a = 15.0573(5) b = 15.0573(5) c = 11.3014(4)	α = 90 β = 90 γ = 120	It emits bright green luminescence at low temperatures	68
40	$[[(PW_9O_{34})_2@Ag_{72}S(S^iPr)_{42}(CF_3COO)_7(CH_3OH)]\cdot 3CF_3COO]$	PI-BIPY	3 D	$P\bar{1}$	a = 28.6218(5) b = 29.0199(5) c = 30.1817(4)	α = 74.6514 (14) β = 78.6648(13) γ = 89.7670(14)	Inter-cluster transformation	81
41	$[Ag_{12}(S^tBu)_6(CF_3COO)_6(DMAC)_{12}]$	CPPP	3 D	*I*2/*m*	a = 16.1359(3) b = 26.5530(5) c = 18.7211(4)	α = 90 β = 95.692(2) γ = 90	Matrix coordination-induced emission	82
42	$[Ag_{12}(S^tBu)_6(CF_3COO)_6]$	NH_2-BPZ	2 D	*P*6/*mmm*	a = 23.5654(5) b = 23.5654(5) c = 11.2007(3)	α = 90 β = 90 γ = 120	Nitrobenzene sensing	83
43	$[Ag_{12}(S^tBu)_6(CF_3COO)_6]$	TPPA	2 D	$P\bar{3}$	a = 43.8008(6) b = 43.8008(6) c = 11.1753(4)	α = 90 β = 90 γ = 120	Exhibit long-lived afterglow emission	84
44	$[Ag_{12}(S^tBu)_6(CF_3COO)_6]$	TPSBF	3 D	$Pn\bar{3}n$	a = 37.941 b = 37.941 c = 37.941	α = 90 β = 90 γ = 90	Sensor for Hg^{2+} ions	61

substituting the vertex-coordinated CH_3CN ligands with various variable-length bidentate *N*-heteroaromatic ligands.[52] Additionally, Bakr and co-workers showcased how the stability of Ag_{16} NCs gradually increases with dimensionalities.[44] These collective findings underscore the significance of transitioning from individual NCs to framework-based structural architectures, which notably enhances stability compared to their isolated counterparts. Given that CAMs arise from the combination of cluster nodes and organic linkers, the discussion turns to the geometry of cluster nodes influenced by the electronic and steric effects of protecting ligands and linkers. Through a coordination assembly approach, linkers of diverse sizes and configurations orchestrate the connection of Ag NCs into intricate 1D, 2D, and 3D designs.

3. Structural features of Ag(I) CAMs

In the quest to establish robust structure–property correlations, a profound understanding of the intricate structural features inherent in Ag(I) CAMs is paramount. These CAMs possess a remarkable capability to finely modulate their structural architectures through the precise manipulation of linker molecules. As Ag cluster nodes intricately bind with organic linker molecules, they orchestrate frameworks with diverse dimensionalities. By carefully altering these linker molecules based on their structural geometry, electronic properties, and steric effects, a plethora of structural architectures can be realized. This discussion aims to delve into the nuanced interplay between linker molecules and silver cluster nodes, illustrating how this interplay governs the evolution of structural frameworks in Ag(I) CAMs, supported by compelling examples and evidence. Beginning with the exploration of Ag(I) CAMs based on BPY, it is intriguing to note that the reports indicate the adoption of various dimensions, such as 1D, 2D, and 3D architectures, despite the utilization of the same protecting ligand, $-S^tBu$. This observation underscores the multifaceted role played not only by linker molecules, but also by solvents in directing the overall architecture of Ag(I) CAMs. For instance, $[Ag_{10}(S^tBu)_6(CF_3CF_2COO)_4(BPY)_2(CH_3CN)_2]_n$ crystallizes in the triclinic space group $P\bar{1}$, establishing a capsule-like $Ag_{10}S_6$ core (Fig. 3a).[66] The structural composition of the Ag_{10} skeleton reveals that it comprises three discernible layers of Ag atoms: both the upper and lower layers consist of three Ag atoms each, while the middle layer takes on a parallelogram-like shape composed of four Ag atoms. Then each surface is protected with *tert*-butyl thiolates, CH_3CN, and $CF_3CF_2COO^-$ anions. The cores interconnect *via* BPY linkers, giving rise to a linear 1D chain (Fig. 3b). Conversely, a strategic alteration in solvent composition, transitioning from acetonitrile to a combination of ethanol/acetone, coupled with the incorporation of a multidentate phenylphosphonic acid ($PhPO_3H_2$) serving as a

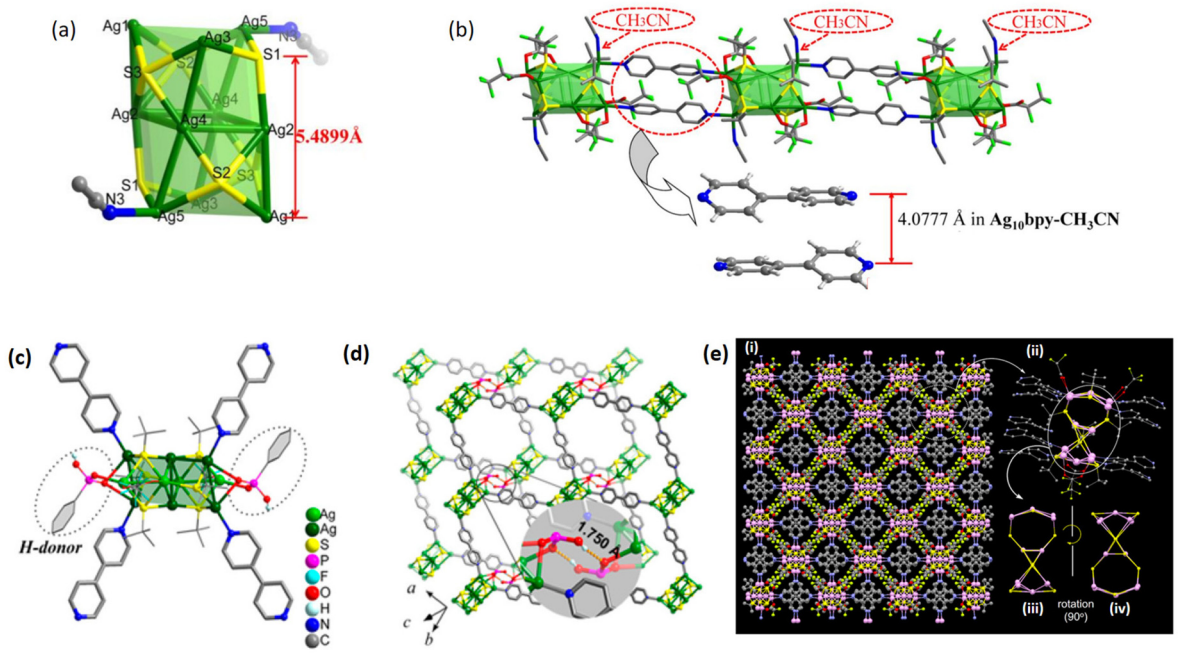

Fig. 3 (a) Capsule-like $Ag_{10}S_6$ core in Ag_{10}BPY-CH_3CN CAM and (b) 1D chain constructed using $Ag_{10}(S^tBu)_6(CF_3CF_2COO)_4$ clusters bridged by BPY. Reprinted from ref. 66 Copyright©2018, Science China Press and Springer-Verlag GmbH Germany. (c) Perspective view of the coordination environment of the $Ag_{10}(S^tBu)_6$ core in Ag_{10}BPY and (d) two-layer stack of the host framework of Ag_{10}BPY with complementary hydrogen bonding (O–H···O, H···O distance is 1.750 Å) between interlayer $-PO_2OH$ moieties. Reprinted with permission from ref. 46 Copyright©2018, American Chemical Society. (e) $[Ag_{12}S_2(S^tBu)_8(CF_3COO)_4(BPY)_8]$ CAM: (i) complete crystal structure, (ii) crystal structure of the monomeric unit $[Ag_{12}S_2(S^tBu)_8(CF_3COO)_4(BPY)_8]$, and (iii and iv) inner silver sulfide cores ($Ag_{12}S_{10}$) without ligands having a C_4 symmetry. Reprinted with permission from ref. 68 Copyright©2022, American Chemical Society.

functional H-bond donor, leads to the formation of the 2D $[Ag_{10}(S^tBu)_6(CF_3COO)_2(PhPO_3H)_2(BPY)_2]_n$ CAM.[46] Despite the pretty similarity in the geometric architecture, crystal system, and space group with the previously mentioned CAMs, the substitution of multidentate phenylphosphonic acids for linear acetonitrile molecules engenders a profound change in the linkage of the BPY linker with the cluster core, resulting in the implementation of a 2D framework (Fig. 3c and d). Additionally, another report describes the adoption of a 3D framework architecture by Ag(I) CAMs utilizing the same BPY linker, albeit with an acetonitrile and methanol solvent mixture, formulated as $\{[Ag_{12}S_2(S^tBu)_8(CF_3COO)_4(BPY)_8]\cdot BPY\}_n$, crystallizing in the orthorhombic space group $I222$.[68] $Ag_{12}S_{10}$ clusters exhibit a dumb-bell-shaped configuration, comprising Ag_5S_4 moieties at the top and bottom and an Ag_2S_2 moiety in the middle. Each Ag_{12} cluster node is stabilized by eight $-S^tBu$ and four CF_3COO^- ligands.

Moreover, eight bidentate BPY ligands, precisely arranged in a square planar bilayer pattern, facilitate the connection between adjacent cluster nodes. This specific arrangement culminates in the formation of an expansive 3D polymeric honeycomb-like structure, showcasing the intricate interplay between ligands and cluster nodes (Fig. 3e). Moreover, investigations into Ag_{10} CAMs have revealed alterations in dimensionality from 1D to 2D based on the linker molecule employed, exemplified by $[Ag_{10}(CF_3COO)_4(S^tBu)_6(4\text{-PCH})_2(CH_3CN)_2]_n$ and $[Ag_{10}(CF_3COO)_4(S^tBu)_6(3\text{-PCH})_4(CH_3CN)]_n$.[79] This highlights the pivotal role of linker molecules in dictating CAM dimensionality. Furthermore, studies involving BPE linkers elucidate the formation of 1D zigzag chains or 3D architectures influenced by the linker concentration (Fig. 4a and b). The synthesis of $[Cd_6Ag_4(SPh)_{16}(DMF)(H_2O)(BPE)]_n$, adopting a 1D zigzag chain, represents a compelling example of strategic linker manipulation.[69] This CP was constructed through the strategic replacement of terminal-coordinated solvent molecules (DMF or CH_3OH) linked to the four terminal Cd atoms of the supertetrahedral chalcogenolate cluster $Cd_6Ag_4(SPh)_{16}(DMF)_3(CH_3OH)$ with a potent electron-donor ligand, BPE. This effectively attached two BPE linker molecules to the two terminal Cd atoms, forming a 1D zigzag chain. Interestingly, by introducing an excess of the rigid BPE linker while maintaining the synthetic strategy, a transition from a 1D to a 3D CP $[(Cd_6Ag_4(SPh)_{16}(BPE)_2)]_n$ was achieved.[70] In this scenario, the excess linker connects all four terminal Cd atoms, facilitating the formation of a 3D architecture (Fig. 4c).

Similarly, the construction of 1D and 2D Ag(I) CAMs using the AZBPY linker amidst specific solvent environments varied electronic and steric effects of thiolate-based protecting ligands, underscoring the versatile nature of linker manipulation. For instance, in a DMF solvent medium and utilizing an adamantanethiolate ($AdmS^-$) protecting ligand, a 1D Ag(I) CAM $[Ag_{11}(AdmS)_6(CF_3COO)_4(AZBPY)_2(DMF)_2][NO_3]$ was

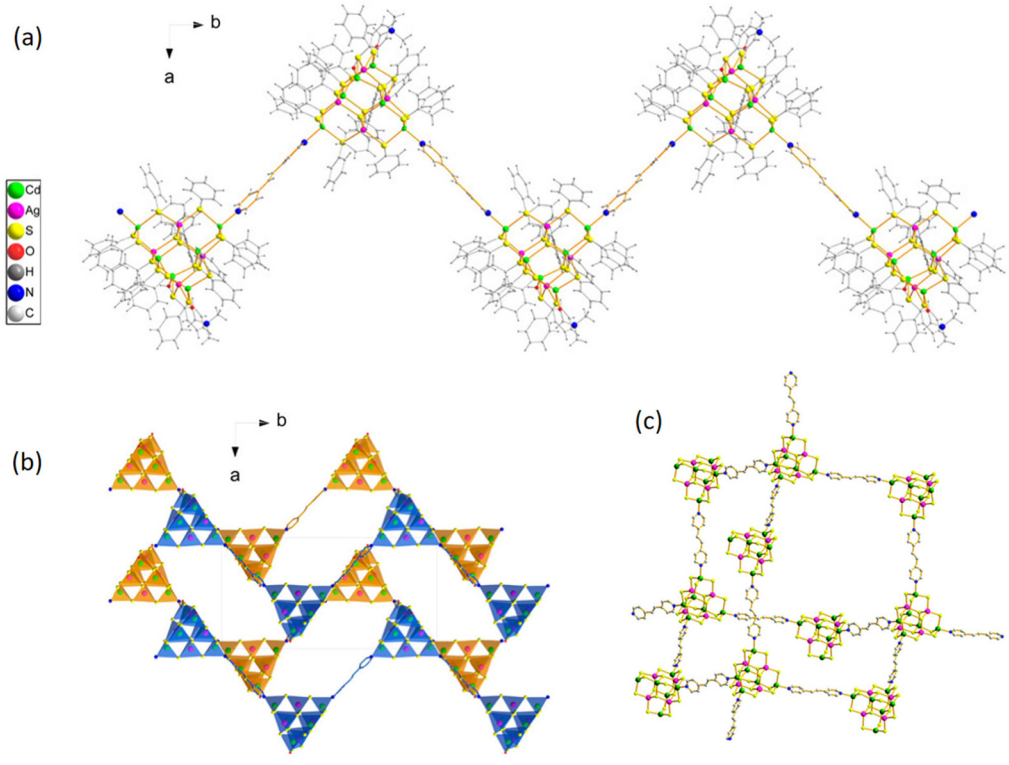

Fig. 4 (a) 1D zigzag chain of $[Cd_6Ag_4(SPh)_{16}(DMF)(H_2O)(BPE)]_n$ and (b) view of $[Cd_6Ag_4(SPh)_{16}(DMF)(H_2O)(BPE)]_n$ in a unit cell from the *ab* plane. Reprinted with permission from ref. 69 Copyright©2020, American Chemical Society. (c) $[Cd_6Ag_4(SPh)_{16}(BPE)_2]$ CAM structure (green, Cd; pink, Ag; yellow, –SPh; red, oxygen; blue, nitrogen; grey, carbon). Reproduced from ref. 70 with permission from the Royal Society of Chemistry.

obtained.[47] In this context, the structural intricacies of the Ag_{11} core manifest in its distinctive distorted elongated square-bipyramid geometry, reminiscent of a Johnson solid, specifically the J_{15} configuration. Notably, this unique geometry accommodates an additional silver atom, further enhancing the complexity and diversity of the core structure. Surrounding this core, a precise arrangement of ligands ensures structural integrity and stability. Specifically, six $AdmS^-$ ligands, four CF_3COO^- ligands, and two DMF molecules encapsulate the Ag_{11} core, providing a robust scaffold for its architecture (Fig. 5a and b). Moreover, the interconnection of Ag_{11} cluster nodes plays a pivotal role in shaping the overall structure of the CAM. Each Ag_{11} cluster node intricately assembles with two adjacent nodes through the AZBPY linker, meticulously constructing a 1D channel-like periodic structure. This precise arrangement not only reinforces the structural integrity of the CAM, but also imbues it with unique architectural features. In contrast, when employing a $-S^tBu$-protecting ligand in a DMAC solvent medium, a distinct 2D Ag(I) CAM emerges with a structural formula $[Ag_{12}(S^tBu)_6(CF_3COO)_6(AZBPY)_3]$.[62] Notably, this CAM showcases an intriguing hollow cuboctahedral geometry, a structural motif known for its stability and architectural versatility. Within this framework, the Ag_{12} core is shielded by six $-S^tBu$ and six CF_3COO^- ligands, forming a protective shell that reinforces structural integrity (Fig. 5c–e). Furthermore, the arrangement of cluster nodes in this 2D CAM facilitates the formation of a layered framework. Each cluster node establishes connections with adjacent nodes through the AZBPY linker molecule, orchestrating a cohesive interaction network that defines the 2D architecture. Indeed, intriguing observations have unveiled instances where altering linker molecules while maintaining fixed thiolate ligands yields CAMs with similar cluster nodes and dimensionality.

Let us further probe into these compelling examples of Ag(I) CAMs. Utilizing a diverse range of organic linkers including BPY, BPY-NH_2, TPyP, Py, and NH_2-BPZ, distinct Ag_{12} CAMs have been synthesized.[68,75,77,83] Remarkably, despite variations in the linker molecules employed, the Ag_{12} core of these CAMs exhibit a strikingly similar hollow cuboctahedral geometry and an overall 2D framework architecture (Fig. 6). However, it is noteworthy that the number of thiolate-protecting ligands and auxiliary ligands may not be uniform across all the 2D Ag_{12} CAMs. This indicates the inherent flexibility in CAM construction, where identical dimensionality can be achieved through diverse ligand arrangements, often offering intriguing insights into structural versatility. Moreover, the adaptability of CAM synthesis extends to transitioning from a 2D to a 3D architecture by simply altering the linker molecules while maintaining a constant thiolate-protecting ligand, particularly $-S^tBu$. For instance, $[Ag_{12}(S^tBu)_6(CF_3COO)_6(TPSBF)_6]_n$ serves as a compelling example of this phenomenon. In this CAM, the TPSBF linker molecule orchestrates the construction of a 3D Ag_{12} CAM while preserving a core geometry reminiscent of its 2D counterparts. Remarkably, $[Ag_2(PhPO_3H)_2(AZBPY)_2]$ is the smallest thiol-free CAM known in the literature.[85] In summary, the complex interplay among linker molecules, solvents, and thiolated ligands profoundly shapes the dimensionality and structural features of Ag(I) CAMs. These observations highlight the nuanced relationship between these factors, providing valuable insights for customized material design and engineer-

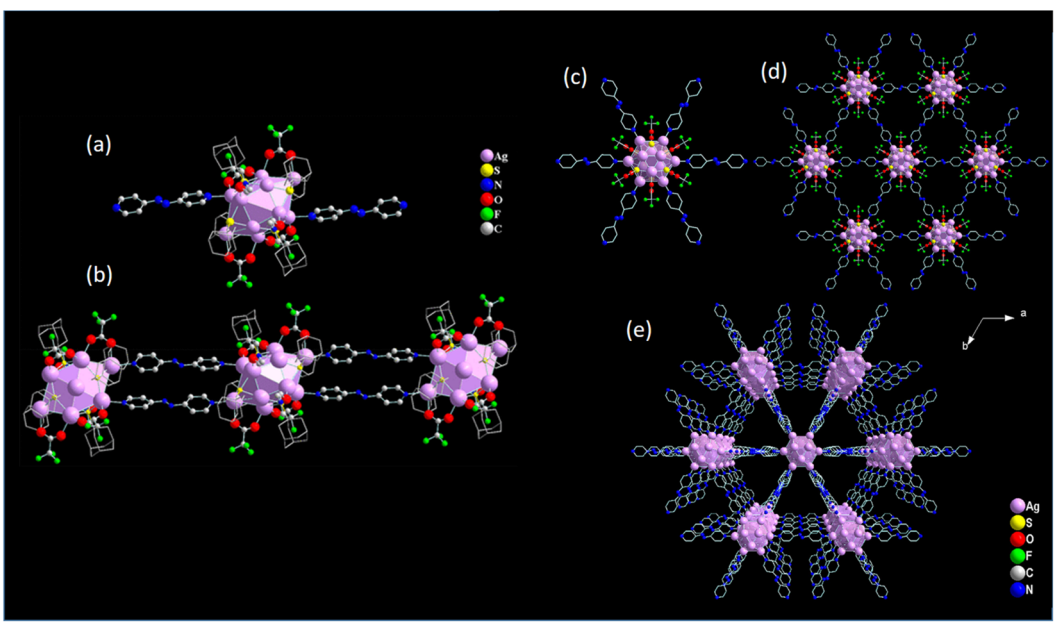

Fig. 5 (a) Repeating unit of $[Ag_{11}(AdmS)_6(CF_3COO)_4(AZBPY)_2(DMF)_2][NO_3]$ and (b) growth of the one-dimensional framework. Reprinted with permission from ref. 47 Copyright©2021, American Chemical Society. (c) Ag_{12} node of $[Ag_{12}(S^tBu)_6(CF_3COO)_6(AZBPY)_3]$ connected with AZBPY linkers, (d) Honeycomb-like hexagonal architecture along the *ab* plane and (e) stacking of the two-dimensional network structure along the *c* axis in an *AAAA* fashion. Reprinted with permission from ref. 62 Copyright©2023, American Chemical Society.

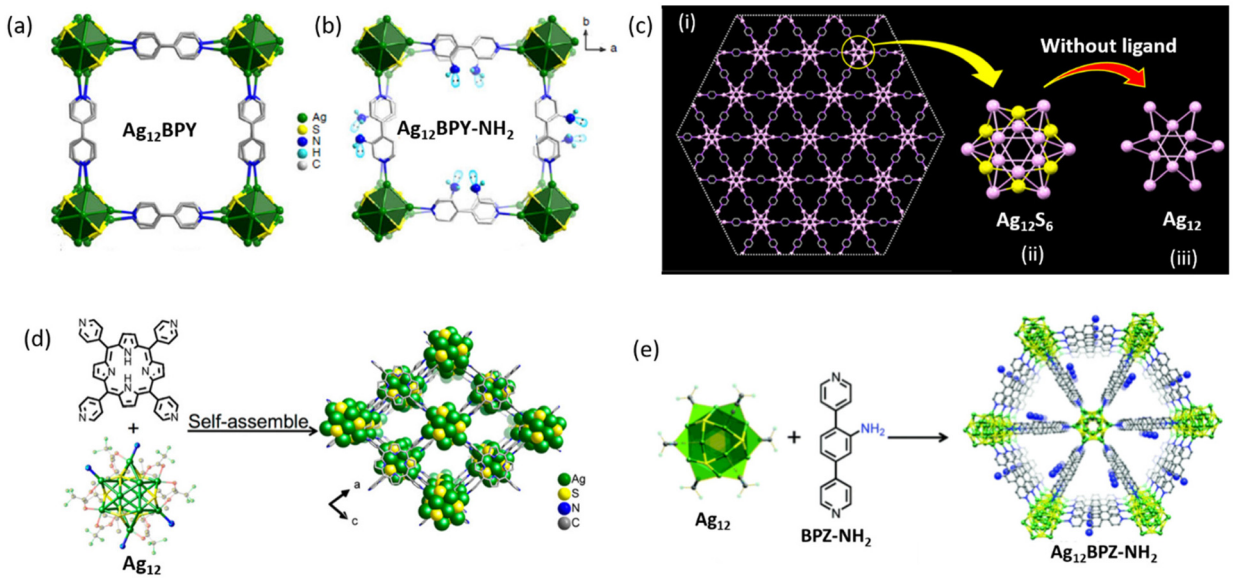

Fig. 6 (a and b) Structures of Ag_{12}BPY and Ag_{12}BPY-NH_2 CAMs based on a hollow Ag_{12} cluster node. Reprinted with permission from ref. 75 Copyright©2020, *Nat. Commun.*. (c) Structure of unit $[Ag_{12}(TBT)_6(TFA)_6(PYZ)_6]$ in the *ab*-plane (i) and structures of the hollow cuboctahedron silver sulfide $Ag_{12}S_6$ core (ii) and (iii) Ag_{12} metallic core without ligands in the *ab*-plane (color codes: Ag, light pink; S, yellow). Reprinted with permission from ref. 68 Copyright©2022, American Chemical Society. (d) Structural unit of $[Ag_{12}(S^tBu)_6(CF_3COO)_3(TPyP)]_n$ CAM made up of a hollow Ag_{12}-cluster node. Reproduced from ref. 77 Copyright©2019, American Chemical Society. (e) Crystal structure of $[Ag_{12}(S^tBu)_6(CF_3COO)_6(NH_2\text{-}BPZ)_3]_n$ based on a hollow Ag_{12}-cluster node. Reproduced from ref. 83 with permission from the Royal Society of Chemistry.

ing. Such versatility in CAM synthesis offers opportunities to tailor their properties, functionalities, and driving innovation across various scientific fields.

Biswas *et al.* unveiled the synthesis of two unprecedented luminescent Ag CAMs, $[Ag_{12}(S^tBu)_6(CF_3COO)_6(TPEPE)_6]_n$ (TUS 1) and $[Ag_{12}(S^tBu)_6(CF_3COO)_6(TPVPE)_6]_n$ (TUS 2), designed with a (4.6)-connected 3D architecture. By ingeniously connecting an Ag_{12} cluster core with quadridentate pyridine linkers, these materials exhibit exceptional fluorescence properties, boasting absolute quantum yields of up to 9.7%.[86] Moreover, their remarkable chemical stability across a wide range of solvent polarities lays the foundation for a highly sensitive Fe^{3+} detection assay with detection limits rivaling industry standards. The detection limits achieved for TUS 1 and TUS 2 are 0.05 and 0.86 nML^{-1}, respectively, rivaling those of conventional standards. The demonstrated efficacy in detecting Fe^{3+} in real water samples underscores the potential of these CAMs in environmental monitoring and assessment, marking a significant stride towards practical applications in diverse fields. Wang *et al.* employed a pyrazine linker to create 1D assemblies of *fcc*-Ag_{14} cluster nodes protected by 1,2-dithiolate-o-carborane.[52] Substituting the linker with AZBPY resulted in a 2D extended framework of the same cluster node. Further innovation with BPY as the linker led to the synthesis of a distinctive 3D framework. The use of variable-length bidentate *N*-heteroaromatic ligands orchestrated the fabrication of 1D-to-3D superatomic CAMs. These findings underscore that the dimensionality of the framework is intricately dictated by the geometric properties of the linkers, transforming the synthetic strategy into a captivating art.

4. Photophysical properties of Ag(I) CAMs

The photoluminescence (PL) studies on Ag(I) CAMs utilizing nitrogen-based bi-multidentate linkers were explored. The covalent interaction between Ag and nitrogen (N) in the assembly often leads to enhanced properties (stability and PL) compared to isolated NCs. Initially, a comparison is made between the molecular clusters and their assembled framework structures to elucidate how the properties of the clusters are tuned. Following this, some examples of the role of guests/solvents on the emission properties are presented. Huang *et al.* reported a $[Ag_{12}(S^tBu)_6(CF_3COO)_6(CH_3CN)_6]\cdot CH_3CN$ NC deteriorating in 30 minutes, which exhibited weak red emission at 620 nm with a quantum yield (QY) of 0.2%.[45] To increase the QY and stability of the NC, they have transformed this NC into a CAM through a ligand exchange approach, *i.e.*, replacing CH_3CN with BPY to produce a $[Ag_{12}(S^tBu)_8(CF_3COO)_4(BPY)_4]_n$ CAM. The as-synthesized CAM exhibited intense emission at 507 nm with a multiple-fold increment in the QY (12.1%). The transition from discrete clusters to the CAM framework immobilized clusters in three dimensions, leading to a significant improvement in stability (stable up to one year) and enhancing the room temperature PL QY (12.1%), which was further utilized as a luminescent sensors. Later on, the same group also investigated the transformation of a singly emissive $[Ag_{12}(S^tBu)_8(CF_3COO)_4(BPY)_4]_n$ CAM into a dual-emissive $[Ag_{12}(S^tBu)_6(CF_3COO)_6(BPY)_3\cdot(DMAC_x\cdot toluene_y)]_n$ CAM (denoted as Ag_{12}BPY-2-solvent) *via* cluster node isomeriza-

tion.[57] The structural conversion from $[Ag_{12}(S^tBu)_8(CF_3COO)_4(BPY)_4]_n$ to Ag_{12}BPY-2-solvent involved a change in the symmetry of the Ag_{12} core from a disconnected D_{2d} 5-2-5 arrangement to a C_{3v} cuboctahedron achieved through solvent selection. The $[Ag_{12}(S^tBu)_8(CF_3COO)_4(BPY)_4]_n$ CAM exhibited weak orange light at room temperature (RT), while Ag_{12}BPY-2-solvent emitted green light (Fig. 7a and b). Interestingly, solvent-free Ag_{12}BPY-2 displayed dual emission (blue and red) with a substantial increase in the low-energy peak (620 nm) by 582-fold and the high-energy peak (463 nm; π and π^* triplet states of BPY) by 17-fold at low temperature (LT). The 620 nm emission in Ag_{12}BPY-2 was attributed to triplet states in the dodenuclear Ag–S cluster nodes of ligand-to-metal–metal charge transfer (LMMCT; S → Ag) character mixed with metal-centered (d*s*/d*p*) states and the emission at 507 nm for $[Ag_{12}(S^tBu)_8(CF_3COO)_4(BPY)_4]_n$ was assigned to inter ligand trans-metallic charge-transfer transitions (ITCT, S/Ag → BPY) and LMMCT (S → Ag) mixed with metal-centered (d*s*/d*p*) transitions. The differences in the geometrical arrangement of the Ag_{12} core resulted in significant changes in the electronic structure and distinct luminescence properties. Enhanced stability and photoluminescence properties were observed from clusters to assembled materials. Alhilaly *et al.* investigated the dimensionality effect on anion-template silver clusters ranging from 0D to 2D, *i.e.*, $[Ag_{16}Cl(S^tBu)_8(CF_3COO)_7(DMF)_4(H_2O)]\cdot1.5(DMF)$ (0D Ag_{16} NC), $[Ag_{15}Cl(S^tBu)_8(CF_3COO)_{5.67}(NO_3)_{0.33}(BPY)_2(DMF)_2]\cdot4.3(DMF)\cdot H_2O$ (1D Ag_{15} NCF), and $[Ag_{14}Cl(S^tBu)_8(CF_3COO)_5(BPY)_2(DMF)]\cdot2(DMF)$ (2D Ag_{14} NCF), observing the loss of a silver atom with an increase in dimensionality.[44] The transition from 1D Ag_{15} NCF to 2D Ag_{14} NCF assembly was controlled by specific precursor ratios. 2D Ag_{14} NCF exhibited emission at 530 nm at RT, while emission from 0D Ag_{16} NC and 1D Ag_{15} NCF was observed only at lower temperatures of around 535 nm. The higher-dimensional structures demonstrated enhanced PL and thermal stability. In a distinct study by Chandrashekar *et al.*, the NC-1 $\{[Ag_{12}(C_6H_{11}S)_6(CF_3COO)_6(C_5H_5N)_6]\cdot4H_2O\}$ demonstrates a cluster-derived emission peak at 605 nm, which undergoes a blue shift to 575 nm at RT in Ag_{12} linked by the TmPyPB linker, forming a two-dimensional assembled framework CAM-1 $\{[Ag_{12}(C_6H_{11}S)_6(CF_3COO)_6(TmPyPB)_2]\cdot(C_4H_8O_2)_3\}$ (denoted as Ag_{12}-TmPyPB CAM).[59] At LT, the emission of NC-1 shifts to 620 nm and the emission of Ag_{12}-TmPyPB CAM also undergoes a red shift to a similar wavelength (625 nm). Spectral envelop deconvolution suggests that the peak shift is associated with the relative intensity of two underlying peaks

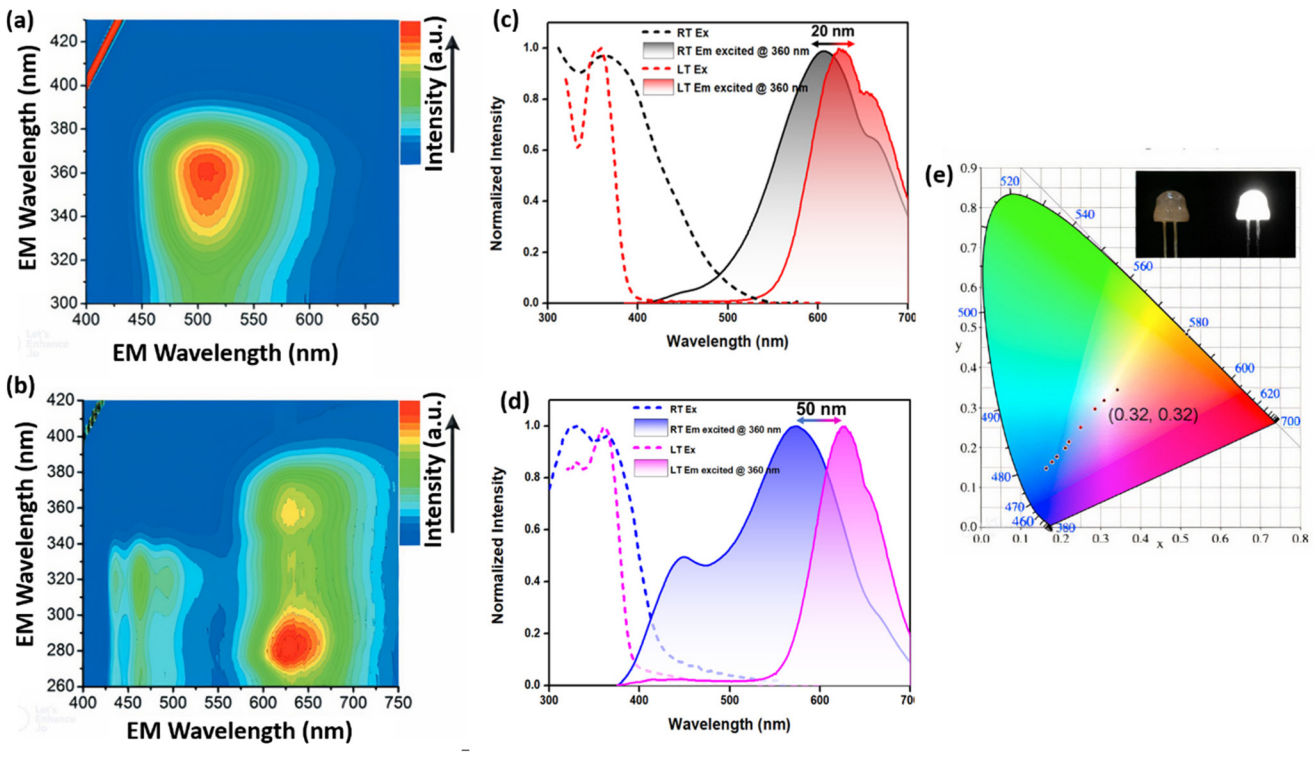

Fig. 7 Three-dimensional excitation–emission matrix (3D-EEM) spectra of (a) Ag_{12}BPY-2 showing emission at 463 and 620 nm and (b) $[Ag_{12}(S^tBu)_8(CF_3COO)_4(BPY)_4]_n$ CAM showing emission at 507 nm. Reproduced from ref. 57 Copyright©John Wiley and Sons. (c) NC-1, excitation spectra probed for the 605 nm emission peak (black dotted line), as well as the emission spectra (black solid line) upon 360 nm excitation at RT. The excitation spectra (red dotted line) probed for 620 nm emission, along with the emission spectra (red solid line) obtained under 360 nm excitation at LT, and (d) CAM-1, excitation spectra (blue dotted line) probed for the 575 nm emission peak, as well as the emission spectra (blue solid line) upon 360 nm excitation at RT. The excitation spectra (magenta dotted line) probed for 625 nm emission, along with the emission spectra (magenta solid line) obtained under 360 nm excitation at LT. Reproduced from ref. 59 with permission from John Wiley and Sons. (e) CIE coordinates of 1 ⊃ DMAC CAM showing guest molecule-induced white light emission. Reproduced from ref. 58 Copyright©2019, Chinese Chemical Society.

resulting from the varying extent of their temperature-dependent populations. Thus, at LT, the emission originating from triplet states (phosphorescence) ($T_1 \rightarrow S_0$) predominates. With an increase in temperature, a reverse population to the S_1 state occurs, and at higher temperatures, the S_1 population becomes dominant. Ag_{12}-TmPyPB CAM with a wider energy gap (ΔE_{ST} = 0.14 eV), requires a higher temperature for reverse intersystem crossing compared to NC-1 (0.06 eV), which has a shorter gap (Fig. 7c and d). These differences in energy gap are attributed to the varying extent of rigidity imparted by the assemblies; NC-1 has supramolecular assembly by non-covalent interactions, while Ag_{12}-TmPyPB CAM was assembled through coordination bonds interconnecting the cluster nodes, giving rise to differences in cluster compression and intra-cluster Ag···Ag interactions within their respective cluster units. Wang *et al.* reported a $PW_9O_{34}^{9-}$ templated Ag_{51} cluster, $[(PW_9O_{34})@Ag_{51}(S)_{25}(CF_3COO)_{17}(DMF)_3(CH_3OH)_3]$ (denoted as SD/Ag51b).[81] This nanocluster underwent a structural transformation by replacing the solvent molecules with bridging pyridine ligands (such as BPY or PI-BIPY), leading to the formation of 2D $\{[(PW_9O_{34})_2@Ag_{72}S(S^iPr)_{41}(CF_3COO)_8(BPY)_{5.5}(CH_3OH)(H_2O)]\cdot 3CF_3COO\}_n$ (denoted as SD/Ag72a) and a 3D framework $\{[(PW_9O_{34})_2@Ag_{72}S(S^iPr)_{42}(CF_3COO)_7(PI\text{-}BIPY)_{4.5}(CH_3OH)]\cdot 3CF_3COO\}_n$ (denoted as SD/Ag72c) structures. Here, structural transformations involving an increase in the nuclearity of the silver cluster from isolated clusters to network formations resulted in different dimensionalities induced by two closely related bipyridine ligands. The solid-state emission of SD/Ag51b and SD/Ag72a occurs in the near-infrared (NIR) region, peaking at 787 nm and 737 nm, respectively, at RT, gradually shifting to 740 nm and 716 nm, respectively at LT. The QY of SD/Ag51b and SD/Ag72a at 113 K was measured to be 1.26% and 2.17%, respectively. These emissions are attributed to ligand-to-metal charge transfer (LMCT) from S/O p to Ag 5 s/p orbitals perturbed by Ag···Ag interactions. In a study by Wu *et al.*, a mesoporous CAM, denoted as 1 ⊃ DMAC, employing the TPPE ligand to form $\{[Ag_{12}(S^tBu)_6(CF_3CO_2)_6(TPPE)_{1.5}](DMAC)_{39}\}$ was developed.[58] This material exhibited blue emission at 454 nm with a QY of 49.9%. Upon exposure to atmospheric conditions, 1 ⊃ DMAC transformed into an empty host framework (referred to as 1) with no DMAC guest molecules in its pores, displaying green emission at 530 nm with a QY of 29.3%. These transformations were reversible, indicating the effective adjustment of luminescence by guest molecules in 1. The cubic cage of 1, with a diameter of 32 Å, facilitated the encapsulation of various guest molecules, leading to observations of circularly polarized luminescence, white-light emission, and room temperature phosphorescence (Fig. 7e). Das *et al.* investigated solvent polarity-induced luminescence studies. They reported a 1D $[Ag_{11}(AdmS)_6(CF_3COO)_4(AZBPY)_2(DMF)_2][NO_3]$ CAM utilizing an AZBPY linker with enhanced emission in acetonitrile, while it remained non-emissive in DMF and chloroform.[47] This phenomenon was attributed to the significant contribution of Ag···S interactions to the occupied molecular orbitals. The thiolate-bounded electrons were found to be influenced by solvent interactions, with the high polarity of acetonitrile effectively affecting the frontier molecular orbitals, thereby resulting in differences in emission behavior in different solvents.

5. Application of Ag(I) CAMs

The synthesis of CAMs encounters challenges that hinder their widespread application. One of the significant bottlenecks lies in the synthesis process, where achieving precise control over the properties of CAMs for targeted applications remains challenging, often due to limitations in the scalability of the synthesis methods.[52,87] While many existing synthesis routes depend on complex procedures, achieving a precise framework structure within a bulk material is essential for exploiting their collective properties effectively. Additionally, understanding the optoelectronic properties of Ag(I) CAMs is highly desirable for various applications, including sensing, device fabrication, *etc*. However, the interplay of complex factors such as shape, size, composition, and protecting organic ligands makes it challenging to fully understand the optoelectronic properties of Ag(I) CAMs.[42]

The utilization of Ag(I) CAMs in biomedical applications, such as drug delivery and imaging, and their biocompatibility and potential off-target toxicity are critical considerations.[78] Silver is known for its antimicrobial properties. However, excessive exposure to silver-based materials may pose risks to human health and the environment.[88] For their safe use in biomedical applications, a thorough investigation is essential to understand their interaction with the biological unit. Researchers worldwide are tackling these existing problems by reporting innovative approaches in synthesis, assembly, and characterization, coupled with a deeper understanding of the fundamental properties of Ag(I) CAMs, which are essential for unlocking the full potential of these materials.[45,61,76] With this context, in this section, we have discussed the utilization of Ag (I) CAMs in various areas such as sensing, biomedical, catalysis, and device fabrication. These could aid the reader in designing and synthesizing Ag(I) CAMs for targeted applications by tuning the reaction conditions.

5.1. Sensing

The prominence of Ag(I) CAMs is steadily increasing within the realm of sensing research. This can be credited to their fluorescence characteristics, uniform distribution, high stability, and adaptability for tailored detection of specific targets. Recently, Das *et al.* reported two $[Ag_{14}(S^tBu)_{10}(CF_3COO)_4(BPA)_2]_n$ and $[Ag_{12}(S^tBu)_6(CF_3COO)_6(BPEB)_3]_n$ CAMs for the detection of label-free DNA.[76] The intricate linker structures combined with the electrostatic interactions between the positively charged CAMs and the negatively charged DNA endow this material with a remarkable capability to mitigate the pronounced background fluorescence emanating from single-stranded (ss) DNA probes labeled with SYBR Green I nucleic acid stain. This innovative feature results in a substan-

tially reduced signal-to-noise ratio, facilitating the detection of label-free target DNA with high precision. Later on, Nakatani *et al.* have presented a novel surface-enhanced Raman scattering sensor based on a three-dimensional Ag(I) cluster-assembled material denoted as $[Ag_{12}(S^tBu)_6(CF_3COO)_6(TPSBF)_6]_n$ for the detection of Hg^{2+} ions.[61] The optical properties of this material are intricately linked to its structural arrangement. This material exhibits remarkable atomic specificity and a unique structural architecture, leading to an exceptionally low detection limit of 0.07 pg mL^{-1} attributed to the formation of the Ag–Hg fusion. Dong *et al.* employed the $[Ag_{12}(S^tBu)_8(CF_3COO)_4(BPY\text{-}NH_2)_4]_n$ CAM (denoted as $Ag_{12}BPY\text{-}NH_2$) for ultrasensitive ratiometric luminescent oxygen sensing, leveraging both dual fluorescence and phosphorescence emission.[89] The introduction of the amino group, featuring lone-pair electrons, effectively initiates spin–orbit coupling, thereby facilitating the triplet excitation state and resulting in dual emission, thus extending the lifetime values. Their findings underscore the exceptional capabilities of the synthesized CAM in detecting oxygen levels even under hypoxic conditions, achieving an impressive sensitivity with a detection limit as low as 0.1 ppm and a rapid response time of 0.3 seconds. This swift response time allows for immediate visual confirmation of oxygen levels, making it a promising tool for practical applications with straightforward observation with the naked eye. In line with this advancement, Li *et al.* contributed to this evolving landscape by elucidating the remarkable reversible photoluminescence dynamics exhibited by $[Ag_{10}(S^tBu)_6(CF_3CF_2COO)_4(BPY)_2(CH_3CN)_2]_n$ (denoted as $Ag_{10}BPY\text{-}CH_3CN$) for acetonitrile sensing.[66] Their results reveal the intriguing property of this one-dimensional Ag(I) CAM chain to emit bright green light centered at 526 nm, while also revealing its sensitivity to environmental factors. Notably, exposure to air leads to a gradual decline in emission intensity, yet the presence of acetonitrile vapor prompts a swift and repeatable restoration of luminescence properties. Dar *et al.* developed an $\{[(Ag_{12}S_2(S^tBu)_8(CF_3COO)_4(BPY)_8)]\cdot BPY\}_n$ CAM (denoted as $Ag_{12}S_2BPY$ CAM)-based luminescence sensor for precise identification of explosive analogs, specifically 2-NT and 2,4-DNT.[68] They observed fluorescence quenching when the vapor of aromatic nitro compounds (2-NT and 2,4-DNT) was exposed to thin films of the CAM, while exposure to aliphatic nitro compounds' vapors showed no change in emission intensity, indicating the material's aptitude for sensing aromatic amines (Fig. 8a–c). Additionally, they successfully reused the synthesized CAM-based sensor multiple times by subjecting the exposed thin film to drying at 45 °C.

5.2. Biomedical

Cao *et al.* reported a new silver-porphyrinic cluster-assembled material $[Ag_9(^tBuC{=}C)_6(CF_3COO)_3(AgTPyP)]_n$, denoted as Ag_9-AgTPyP.[78] They demonstrated its potential application in bioprotection against super bacteria under visible light (Fig. 9a–c). Through mechanistic inquiries, they uncovered that the combined presence of silver clusters and porphyrin units within the framework significantly bolstered the material's capacity for charge separation upon photoexcitation, consequently activating oxygen molecules to generate reactive oxygen species such as singlet oxygen ($^1O_2$), superoxide radicals ($^{\bullet}O_2^-$), and hydrogen peroxide (H_2O_2). Notably, they identified a novel long-term charge-transfer process from the AgTPyP unit to adjacent Ag_9 clusters. Additionally, they observed that the Ag_9 cluster exhibited a pronounced affinity towards oxygen molecules, thereby enhancing the efficiency of reactive oxygen species production. Das *et al.* explored the applicability of the newly synthesized two-dimensional $[Ag_{14}(S^tBu)_{10}(CF_3COO)_4(AZBPY)_2]_n$ CAM in photoacoustic imaging.[65] They have investigated the photoacoustic wave generation capabilities of the synthesized CAM in various solvent media and the obtained results showed that the ethanol/chloroform medium induced more interactions, particularly C–H···F interactions with cluster units, compared to the ethanol/acetonitrile medium. This interaction altered the interdependent radiative photon emission and non-radiative phonon emission processes. Notably, ethanol/acetonitrile demonstrated superior blood vessel mimicking ability with the synthesized nanoclusters, attributed to its enhanced photoacoustic wave generation capability.

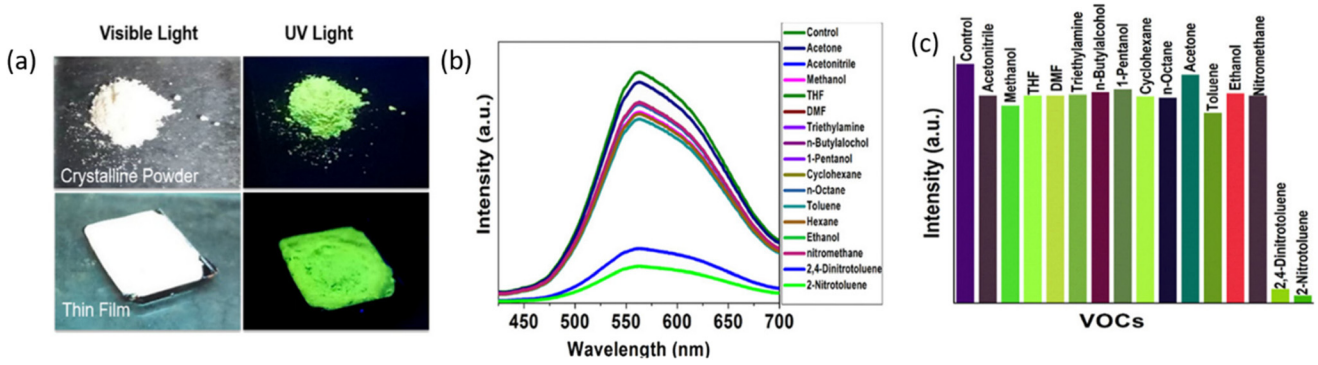

Fig. 8 (a) Photographs exhibiting the CH_3CN vapor-induced photoluminescence changes of the sample $Ag_{10}BPY\text{-}CH_3CN$: photographs of the crystalline powder and thin film of $Ag_{12}S_2BPY$ CAM under visible and UV light, (b) PL spectra of thin films of $Ag_{12}S_2BPY$ CAM independently exposed to the vapors of various organic molecules excited at 370 nm and (c) Bar diagram showing the sensitivity of thin films of $Ag_{12}S_2BPY$ CAM exposed to the vapors of different solvents. Reprinted with permission from ref. 68 Copyright©2022, American Chemical Society.

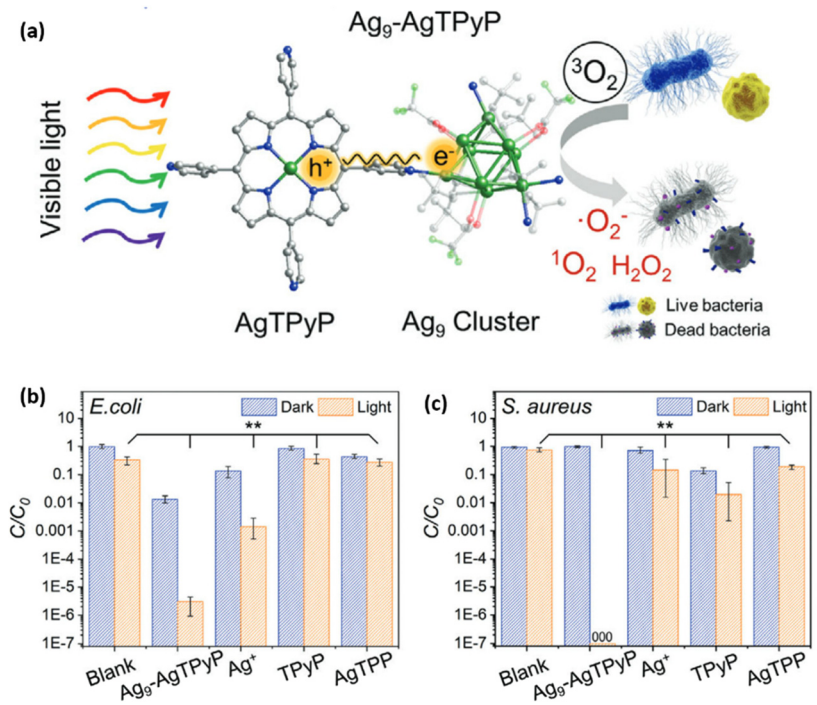

Fig. 9 (a) Schematic representation of the Ag_9-AgTPyP photocatalytic inactivation of antibiotic-resistant bacteria. Antibacterial properties of Ag_9-AgTPyP. Comparison of the photocatalytic antibacterial performances of Ag_9-AgTPyP, Ag^+, TPyP, and AgTPP under both light and dark conditions on (b) *E. coli* and (c) *S. aureus* (**$p < 0.01$). Reprinted with permission from ref. 78 Copyright©2021, Advanced Science.

5.3. Catalysis

Ag(I) CAMs have been gaining popularity as catalysts, primarily due to their ability to generate reactive species such as $^1O_2$, higher stability over several cycles of catalysis, and generation of active sites for substrate binding. The generation of $^1O_2$ *via* photosensitization of the porphyrinic-based CAM has proven instrumental in neutralizing warfare agent simulants such as the mustard gas simulant 2-chloroethyl ethyl sulfide (CEES) and the neuro agent simulant diethyl cyanophosphonate (DECP).[77,90,91] Cao *et al.* have synthesized $[Ag_{12}(S^tBu)_6(CF_3COO)_3(TPyP)]_n$ (Ag_{12}TPyP) which by its porous structure could capture an incremental amount of CEES and oxidize it to a less harmful $CEESO_2$ with 100% selectivity.[77] They have also reported two phosphate-templated CAMs, namely $[(HPO_4)_4(H_2PO_4)_2@Ag_{54}(S^iPr)_{32}(CF_3COO)_6(CH_3CN)_2(H_2TCPP)(TCPP)]_n$ (ZZU-601) and $\{[(HPO_4)_2@Ag_{18}(S^iPr)_8(H_2PO_4)_4(H_2ZnTCPP)(C_2H_5OH)]_2CH_3CN\}_n$ (ZZU-602), which proved to be effective not only against CEES, but also DECP as well.[90] Zhang *et al.* showed further modification in the Ag_{12} nanocluster to synthesize 4 different CAMs with modified BODIPY ligands, such as Ag_{12}-BDP, Ag_{12}-BDP-Py, Ag_{12}-BDP-H, and Ag_{12}-BDP-I, in the quest to meticulously modulate its porosity, $^1O_2$ generation efficiency, and adsorption (Fig. 10a).[91] Meanwhile, all of them showed good conversion efficiency against CEES, and Ag_{12}-BDP-I demonstrated the best performance owing to the presence of two heavy iodine atoms at 2 and 6 positions, which facilitated ISC and hence $^1O_2$ generation.

The narrow band gap of metal chalcogenolate clusters has paved the way for photocatalytic degradation of organic dyes.[55,70] Xu *et al.* have synthesized a ternary chalcogenolate cluster $Cd_6Ag_4(SPh)_{16}(DMF)_4$ and its 3D $\{[Cd_6Ag_4(SPh)_{16}](BPE)_2\}$ CAM connected by the rigid BPE linker.[92] While the molecular cluster itself took 180 min to reduce the concentration of rhodamine B (RhB) by 95% under illumination, the framework achieved the same in 90 min (Fig. 10b). The conjugated structure of RhB was degraded, evident from the red shift in the absorbance upon successive illumination. The framework nature and the broad visible spectra could efficiently use the incoming energy. To further delve into the degradation mechanism of RhB, Wang *et al.* synthesized a 1D Ag(I) CAM chain, $[Cd_6Ag_4(SPh)_{16}(DMF)(H_2O)(BPE)]_n$, with a broader and red-shifted (120 nm) absorption spectra than the parent $Cd_6Ag_4(SPh)_{16}(DMF)_4$ cluster.[93] It reduced the concentration of RhB by 98% in 20 min after illumination, showcasing superior photocatalytic potential than its parent cluster, even after 5 cycles of catalytic activity. When investigating its degradation activity in the presence of several scavengers, they observed a suppression upon the addition of NaN_3 (the $^1O_2$ scavenger). It was concluded that $^1O_2$ is the primary species for the degradation of the dye. Moreover, when the reaction was performed under N_2 conditions, similar observations were made owing to the absence of O_2 and hence the generation of $^1O_2$. The conjugated structure of the chain facilitated better optical absorption, generating charge carriers and facilitating their movement on the catalyst, thereby generating $^1O_2$ to degrade RhB.

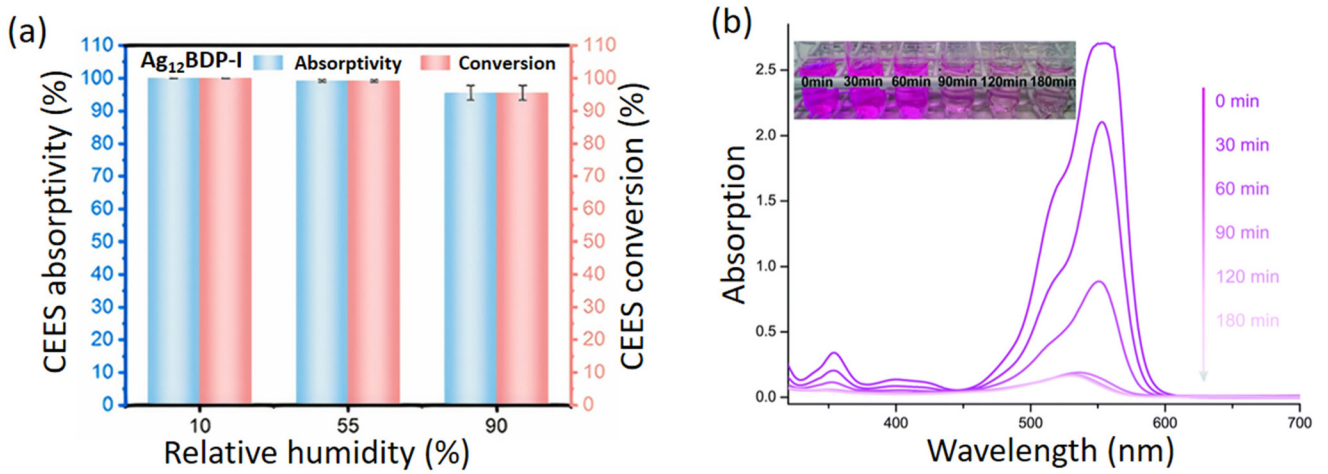

Fig. 10 (a) Absorptivity and conversion of gaseous CEES in the presence of Ag_{12}-BDP-I CAM. Reprinted with permission from ref. 91 Copyright©2023, American Chemical Society. (b) UV/vis spectra and color images showing the decomposition of aqueous rhodamine B (4.2×10^{-5} M) photocatalyzed by the microporous $[Cd_6Ag_4(SPh)_{16}(DMF)(H_2O)(BPE)]_n$ CAM. Reproduced from ref. 70 with permission from the Royal Society of Chemistry.

The π-Lewis acidic nature of the Ag(I) atoms has been harnessed in organic catalytic reactions to undertake carboxylate cyclization of both terminal and internal propargyl amines with CO_2. The extraordinary substrate scope was achieved through the arrangement of the saddle-shaped Ag_{27} nanocluster into a 2D structure connected *via* TPyP-H_2 ligands to synthesize a $\{[Ag_{27}S_2(S^tBu)_{14}(CF_3COO)_8(TPyP\text{-}H_2)][(CF_3COO)\}_n$ CAM that maximized the accessibility of the substrate and exposed Ag atoms for efficient binding *via* Ag–π interactions.[94] Jing *et al.* utilized an enantiomeric mixture of R/S-$[Ag_{17}Cl(S^iPr)_9S(CH_3COO)_5H_2O]$ (R/SAg_{17}), alongside [Ir(coumarin)$_2$(DTBBPY)][PF_6] as a photosensitizer (PS) and triethanolamine (TEOA) as a sacrificial electron donor in a three-component hydrogen-evolving catalytic system.[8] After 8 h of photocatalysis, they successfully generated 547.9 μmol of hydrogen gas with a TON of ~4440, which excels more than most of the reported silver-based photocatalysts for hydrogen evolution. The framework nature of the cluster caters to it with higher stability to perform better as a catalyst than compared 0D clusters known in the literature.

5.4. Device fabrication

Since the revelation of layered carbon nanomaterials, scientists have turned towards atomically stacked 2D nanostructures.[95,96] When these materials are scaled down to a single layer, they undergo profound alterations in optical properties, charge carrier mobility, and electrical conductivity, all attributable to quantum size effects.[96,97] This transformative capability positions 2D semiconductor materials at the forefront of advanced electronic device design.[98] Field-effect transistors (FETs) are pivotal components of modern technological devices, operating as three-terminal devices where the voltage applied to the gate terminal controls the electric current flow through the channel.[99] 2D semiconductors have emerged as ideal candidates for transistors, overcoming challenges such as channel shrinking encountered with silicon transistors.[100] The evolution of atomically precise organic semiconductors presents an intriguing story in the field of FET devices. These materials, characterized by discrete energy levels, offer unparalleled versatility in electronic coupling, allowing for fine-tuning through alterations in size and composition. While colloidal semiconducting quantum dots initially showcased immense promise, their non-deterministic size distribution hindered electronic coupling control.[101] In pursuit of precision and efficiency, researchers redirected their focus toward atomically precise Au-based NCs, harnessing the benefits of discrete energy levels arising from quantum confinement but faced challenges due to inherently resistant colloidal interconnectivity among discrete NCs, affecting the overall charge transport properties.[101] Later on, a separate study highlighted the importance of long-range ordering in enhancing semiconducting transport properties.[102] Yuan *et al.* introduced a 1D $(AuAg)_{34}$(1-ethynyladamantane)$_{20}$ NC assembled *via* Ag–Au–Ag bonds, exhibiting superior carrier mobility compared to previous examples.[103] However, the transport characteristics of pure Ag NCs remain a challenge. By tackling stability concerns, the potential of organized Ag(I) CAMs with precisely designed structural arrangements emerges as a captivating frontier.

The pursuit of a 2D single-layer architecture of Ag(I) CAMs adds a layer of intrigue to this narrative. To pursue a 2D single-layer architecture, researchers have sought towards a top-down approach, *i.e.*, utilizing mechanical vibration on bulk crystals. By delving into the intricate semiconducting transport properties of a single layer of Ag(I) CAMs, Das *et al.* have introduced a synthetic methodology to fabricate an Archimedean solid-like Ag(I) core-based semiconducting CAM, $[Ag_{12}(S^tBu)_6(CF_3COO)_6(AZBPY)_3]$, denoted as Ag_{12}-AZBPY.[62] In this structure, AZBPY linkers selectively bond to Ag_{12} cluster

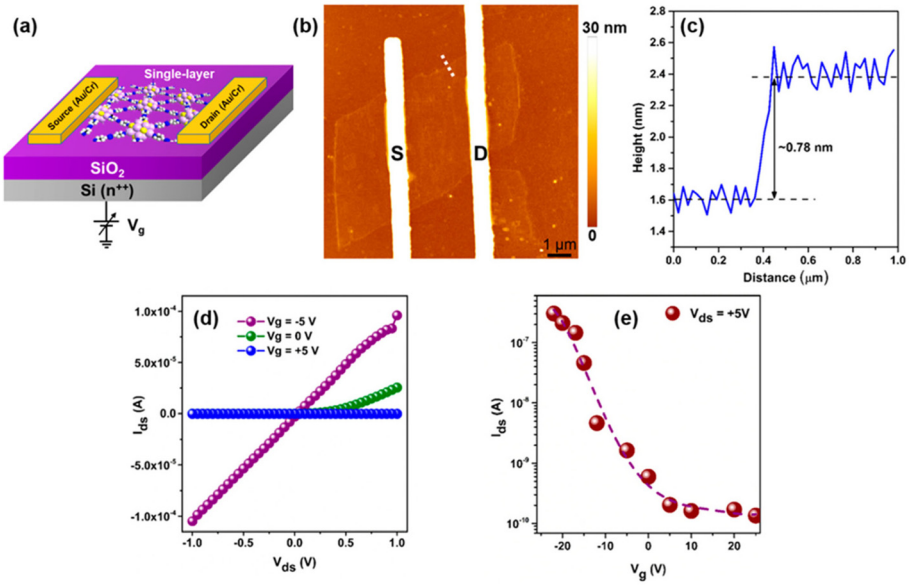

Fig. 11 (a) Schematic representation of the bottom-gated FET measurement. (b) AFM topography of a monolayer Ag_{12}-AZBPY FET device on a SiO_2/Si substrate with two metal contacts serving as a source (*S*) and a drain (*D*) defined on top of the flake. (c) Height profile along the white-dotted line in panel b, (d) source–drain characteristics, and (e) transfer characteristics of a bottom-gated FET device. Reprinted with permission from ref. 62 Copyright©2023, American Chemical Society.

nodes, forming a covalently bonded 2D honeycomb-like layered architecture. Single-crystal analysis unveils a hexagonal crystal structure with interlayer non-covalent stacking, while liquid phase exfoliation yields distinct single layers with finely modulated optoelectronic band structures. The optimized CAM showcases a unique electronic configuration with the conduction band localized on the azo group of the AZBPY linkers and the valence band localized on the Ag_{12} cluster nodes. This arrangement facilitates efficient electron injection into the cluster nodes, albeit with restricted interlayer charge hopping (Fig. 11). Leveraging these properties, they fabricate a FET device utilizing a single-layer Ag_{12} CAM, demonstrating remarkable *p*-type behavior with a hole mobility of 1.215 $cm^2 V^{-1} s^{-1}$ at 5 V, a carrier concentration of 4.98 × 1018 cm^{-3}, and an 'ON/OFF' current ratio of up to 4500 at RT. This underscores the immense potential of 2D Ag(I) CAMs as new materials for semiconductor applications, providing crucial insights into the design and fabrication of electronic devices with unprecedented performance characteristics.

6. Conclusions and future outlook

This comprehensive review summarizes a discussion on the representative studies concerning the assembly formation and structural characteristics of Ag(I) CAMs, highlighting the structure–property correlation. Additionally, we probed into the key factors influencing the dimensionality of the assemblies. Photoluminescence, one of the most prevalent properties of these CAMs, has also been discussed with insights into its temperature-dependent emission and tunability with intricate changes in the structure. These investigations have underscored the remarkable versatility and tunability of Ag(I) CAMs, enabling precise control over their properties for a wide range of applications spanning photoacoustic imaging, sensing, organic dye degradation, syngas generation, and so on. Furthermore, we have meticulously compiled a detailed summary of the unit-cell parameters, space group, dimensionality, and applications of the reported Ag(I) CAMs in the literature presented in a tabular format (Table 1). We believe that the discussion presented herein will prove instrumental for beginners and individuals well-versed in the subject.

7. Future outlook

7.1. Targeted synthesis and dimensionality control

A promising direction for future research could involve refining the precise customization of Ag(I) CAM synthesis, providing us with the ability to finely control their dimensionality. Although significant progress has been made in understanding their structure and properties, there remains a need for a deeper understanding of the assembly process of cluster nodes and linkers. Controlled synthesis techniques are important for tailoring Ag(I) CAMs to specific applications, thus more extensive research in this area is needed to unleash their full potential.

7.2. Photoluminescence mechanism and enhancement

The photoluminescence properties of Ag(I) CAMs have received considerable attention, although unraveling their underlying

mechanisms and improving their photoluminescence quantum yield present significant challenges. Understanding the respective roles of the NC core and organic linker components of the CAMs in emission, as well as identifying excited states contributing to emission (fluorescence and phosphorescence), is crucial for improving the functionality of CAMs across various applications.

7.3. Functional devices and applications

Despite the significant progress in fundamental studies, there is a need for the development of functional devices and applications utilizing Ag(I) CAMs. Promising avenues include field-effect transistors, memory devices, and sensors, leveraging the specific structure architecture of Ag(I) CAMs. Additionally, these have the potential ability for biomedical applications, therefore research in this direction can open the way for state-of-the-art applications of Ag(I) CAMs.

7.4. Healthcare diagnostics and environmental monitoring

The utilization of Ag(I) CAMs in DNA detection and photoacoustic imaging is getting attention. Further research in these directions can increase the selectivity and sensitivity of Ag(I) CAM-based DNA sensors, enabling accurate and early detection of genetic biomarkers associated with various diseases. Additionally, Ag(I) CAMs are emerging as promising sensors for notorious environmental pollutants such as heavy metals and synthetic organic dyes. Future research endeavors could focus on optimizing the design of Ag(I) CAM-based sensors to achieve highly accurate and rapid detection of notorious environmental pollutants, enabling timely identification and mitigation of potential threats.

Abbreviations

CAM	Cluster-assembled material
MOF	Metal–organic framework
NC	Nanocluster
CP	Coordination polymer
PL	Photoluminescence
QY	Quantum yield
S^tBu	*tert*-Butylthiolate
S^iPr	2-Propanethiolate
SEt	Ethanethiolate
SPh	Thiophenolate
AdmS	1-Adamantanethiolate
TBT	*tert*-Butylthiolate
^{t}BuC≡C	*tert*-Butylacetylide
PPh_3	Triphenylphosphine
$AgCF_3COO$	Silvertrifluoroacetate
TFA	Trifluoroacetate
$NaBH_4$	Sodiumborohydride
PYZ	Pyrazine
Py	Pyridine
BPY	4,4′-Bipyridine
BPE	1,2-Bis(4-pyridyl)ethylene
AZBPY	4,4′-Azopyridine
BPY-NH_2	3-Amino-4,4′-bipyridine
TPPE	1,1,2,2-Tetrakis(4-(pyridin-4-yl)phenyl)ethene
TmPyPB	1,3,5-Tris(3pyridyl-3-phenyl)benzene
BPA	1,2-Bis(4-pyridyl)acetylene
BPEB	1,4-Bis(pyridin-4-ylethynyl)benzene
TPyP	[5,10,15,20-Tetra(4-pyridyl)porphyrin]
2-PCH	2-Pyridine carboxylic hydrazide
3-PCH	3-Pyridine carboxylic hydrazide
4-PCH	4-Pyridine carboxylic hydrazide
TPBTC	Benzene-1,3,5-tricarboxylic acid tris-pyridin-4-ylamide
BPA	1,2-Bis(4-pyridyl)ethane
CPPP	2,5-Bis(4-cyanophenyl)-1,4-bis(4-(pyridine-4-yl)-phenyl)-1,4-dihydropyrrolo[3,2-*b*]pyrrole
PI-BIPY	1,4-Bis(4-pyridinylmethyl)piperazine
NH_2-BPZ	1,4-Bis(pyrid-4-yl)benzenenamine
TPPA	Tris(4-pyridylphenyl)-amine
TPP	Tetraphenyl porphyrin
TCPP	Tetrakis(4-carboxyphenyl)porphyrin
TPSBF	2,2′,7,7′-Tetra(pyridin-4-yl)-9,9′-spirobi(fluorene)
POMs	Polyoxometallates
BODIPY	Boron-dipyrromethene derivative
BDP	Boron-dipyrromethene
CEES	2-Chloroethyl ethyl sulfide
DECP	Diethyl cyanophosphonate
DTTBPY	4,4′-Bis(*tert*-butyl)-2,2′-bipyridine
RhB	Rhodamine B
PS	Photosensitizer
TEOA	Triethanolamine
DCM	Dichloromethane
CH_3OH	Methanol
$CHCl_3$	Chloroform
CH_3CN	Acetonitrile
DMF	*N*,*N*-Dimethylformamide
DMAC	*N*,*N*-Dimethylacetamide
HOMO	Highest occupied molecular orbital
LUMO	Lowest unoccupied molecular orbital
LMMCT	Ligand-to-metal–metal charge transfer
LMCT	Ligand-to-metal-charge transfer
ITCT	Inter ligand *trans*-metallic charge transfer
FET	Field-efftect transistors
ISC	Inter-system crossing
1 D	One-dimensional
2 D	Two-dimensional
3 D	Three-dimensional
RT	Room temperature
LT	Low temperature
2-NT	2-Nitrotoluene
2,4-DNT	2,4-Dinitrotoluene
TON	Turnover Number

Conflicts of interest

The authors declare no conflict of interest.

Acknowledgements

P. C. acknowledges the Council of Scientific & Industrial Research India for fellowship.

References

1 S. Biswas, A. K. Das and S. Mandal, *Acc. Chem. Res.*, 2023, **56**, 1838–1849.
2 N. Baig, *Composites, Part A*, 2023, **165**, 107362.
3 Z. Liu, M. Zhou, L. Luo, Y. Wang, E. Kahng and R. Jin, *J. Am. Chem. Soc.*, 2023, **145**, 19969–19981.
4 R. Jin, *Nanoscale*, 2015, **7**, 1549–1565.
5 R. Jin, C. Zeng, M. Zhou and Y. Chen, *Chem. Rev.*, 2016, **116**, 10346–10413.
6 K. Sahoo and I. Chakraborty, *Nanoscale*, 2023, **15**, 3120–3129.
7 A. Gonzàlez-Rosell, S. Malola, R. Guha, N. R. Arevalos, M. F. Matus, M. E. Goulet, E. Haapaniemi, B. B. Katz, T. Vosch and J. Kondo, *J. Am. Chem. Soc.*, 2023, **145**, 10721–10729.
8 X. Jing, F. Fu, R. Wang, X. Xin, L. Qin, H. Lv and G.-Y. Yang, *ACS Nano*, 2022, **16**, 15188–15196.
9 P. Su, B. Tang and F. X. Xiao, *Small*, 2024, **20**, 2307619.
10 Y.-X. Wang, J. Zhang, H.-F. Su, X. Cui, C.-Y. Wei, H. Li and X.-M. Zhang, *ACS Nano*, 2023, **17**, 11607–11615.
11 A. Chakraborty, M. M. Stanley, B. Mondal, M. Bodiuzzaman, P. Chakraborty, M. Kannan and T. Pradeep, *Nanoscale*, 2023, **15**, 2690–2699.
12 Q. Li, S. Yang, J. Chai, H. Zhang and M. Zhu, *Nanoscale*, 2022, **14**, 15804–15811.
13 J. Tang, C. Liu, C. Zhu, K. Sun, H. Wang, W. Yin, C. Xu, Y. Li, W. Wang and L. Wang, *Nanoscale*, 2023, **15**, 2843–2848.
14 H. Wu, R. Anumula, G. N. Andrew and Z. Luo, *Nanoscale*, 2023, **15**, 4137–4142.
15 K. Kuang, C. Zhou, M. Jing, C. Fang, Z. Li, S. Chen and M. Zhu, *ChemElectroChem*, 2024, **11**, e202300503.
16 W. Jing, H. Shen, R. Qin, Q. Wu, K. Liu and N. Zheng, *Chem. Rev.*, 2022, **123**, 5948–6002.
17 R. Jin, G. Li, S. Sharma, Y. Li and X. Du, *Chem. Rev.*, 2020, **121**, 567–648.
18 E. L. Albright, T. I. Levchenko, V. K. Kulkarni, A. I. Sullivan, J. F. DeJesus, S. Malola, S. Takano, M. Nambo, K. Stamplecoskie, H. Häkkinen, T. Tsukuda and C. M. Crudden, *J. Am. Chem. Soc.*, 2024, **146**, 5759–5780.
19 O. López-Estrada, N. Mammen, L. Laverdure, M. M. Melander, H. Häkkinen and K. Honkala, *ACS Catal.*, 2023, **13**, 8997–9006.
20 P. Chakraborty, S. Malola, P. Weis, M. Neumaier, E. K. Schneider, H. Häkkinen and M. M. Kappes, *J. Phys. Chem. Lett.*, 2023, **14**, 11659–11664.
21 C. Dutta, S. Maniappan and J. Kumar, *Chem. Sci.*, 2023, **14**, 5593–5601.
22 Z. Lei, P. Zhao, X.-L. Pei, H. Ube, M. Ehara and M. Shionoya, *Chem. Sci.*, 2023, **14**, 6207–6215.
23 B. Tang, S.-C. Zhu, H. Liang, S. Li, B.-J. Liu and F.-X. Xiao, *J. Mater. Chem. A*, 2022, **10**, 4032–4042.
24 X. Yan, X. Y. Fu and F. X. Xiao, *Adv. Funct. Mater.*, 2023, **33**, 2303737.
25 C. Xu, Y. Jin, H. Fang, H. Zheng, J. C. Carozza, Y. Pan, P.-J. Wei, Z. Zhang, Z. Wei and Z. Zhou, *J. Am. Chem. Soc.*, 2023, **145**, 25673–25685.
26 G. Deng, H. Yun, M. S. Bootharaju, F. Sun, K. Lee, X. Liu, S. Yoo, Q. Tang, Y. J. Hwang and T. Hyeon, *J. Am. Chem. Soc.*, 2023, **145**, 27407–27414.
27 R.-W. Huang, X. Song, S. Chen, J. Yin, P. Maity, J. Wang, B. Shao, H. Zhu, C. Dong and P. Yuan, *J. Am. Chem. Soc.*, 2023, **145**, 13816–13827.
28 V. Truttmann, A. Loxha, R. Banu, E. Pittenauer, S. Malola, M. F. Matus, Y. Wang, E. A. Ploetz, G. n. Rupprechter and T. Bürgi, *ACS Nano*, 2023, **17**, 20376–20386.
29 Y. Du, H. Sheng, D. Astruc and M. Zhu, *Chem. Rev.*, 2019, **120**, 526–622.
30 H. Hirai, S. Ito, S. Takano, K. Koyasu and T. Tsukuda, *Chem. Sci.*, 2020, **11**, 12233–12248.
31 J. F. Corrigan, O. Fuhr and D. Fenske, *Adv. Mater.*, 2009, **21**, 1867–1871.
32 Y. Li, M. Zhou and R. Jin, *Adv. Mater.*, 2021, **33**, 2006591.
33 X. Kang, Y. Li, M. Zhu and R. Jin, *Chem. Soc. Rev.*, 2020, **49**, 6443–6514.
34 Y.-P. Xie, Y.-L. Shen, G.-X. Duan, J. Han, L.-P. Zhang and X. Lu, *Mater. Chem. Front.*, 2020, **4**, 2205–2222.
35 S. Biswas, P. Sun, X. Xin, S. Mandal and D. Sun, *At. Precise Nanochem.*, 2023, 453–478.
36 I. Chakraborty and T. Pradeep, *Chem. Rev.*, 2017, **117**, 8208–8271.
37 Y. Jin, C. Zhang, X.-Y. Dong, S.-Q. Zang and T. C. Mak, *Chem. Soc. Rev.*, 2021, **50**, 2297–2319.
38 Y.-P. Xie, J.-L. Jin, G.-X. Duan, X. Lu and T. C. Mak, *Coord. Chem. Rev.*, 2017, **331**, 54–72.
39 H. Schmidbaur and A. Schier, *Angew. Chem., Int. Ed.*, 2015, **54**, 746–784.
40 Z.-Y. Chen, D. Y. Tam and T. C. Mak, *Nanoscale*, 2017, **9**, 8930–8937.
41 X.-Y. Li, Z. Wang, H.-F. Su, S. Feng, M. Kurmoo, C.-H. Tung, D. Sun and L.-S. Zheng, *Nanoscale*, 2017, **9**, 3601–3608.
42 S. Biswas, S. Das and Y. Negishi, *Coord. Chem. Rev.*, 2023, **492**, 215255.
43 A. Ebina, S. Hossain, H. Horihata, S. Ozaki, S. Kato, T. Kawawaki and Y. Negishi, *Nanomaterials*, 2020, **10**, 1105.
44 M. J. Alhilaly, R.-W. Huang, R. Naphade, B. Alamer, M. N. Hedhili, A.-H. Emwas, P. Maity, J. Yin, A. Shkurenko, O. F. Mohammed, M. Eddaoudi and O. M. Bakr, *J. Am. Chem. Soc.*, 2019, **141**, 9585–9592.
45 R.-W. Huang, Y.-S. Wei, X.-Y. Dong, X.-H. Wu, C.-X. Du, S.-Q. Zang and T. C. Mak, *Nat. Chem.*, 2017, **9**, 689–697.

46 X.-Y. Dong, H.-L. Huang, J.-Y. Wang, H.-Y. Li and S.-Q. Zang, *Chem. Mater.*, 2018, **30**, 2160–2167.
47 A. K. Das, S. Biswas, S. S. Manna, B. Pathak and S. Mandal, *Inorg. Chem.*, 2021, **60**, 18234–18241.
48 X. H. Wu, P. Luo, Z. Wei, Y. Y. Li, R. W. Huang, X. Y. Dong, K. Li, S. Q. Zang and B. Z. Tang, *Adv. Sci.*, 2019, **6**, 1801304.
49 J. Y. Wang, R. W. Huang, Z. Wei, X. J. Xi, X. Y. Dong and S. Q. Zang, *Chem. – Eur. J.*, 2019, **25**, 3376–3381.
50 C. P. Joshi, M. S. Bootharaju and O. M. Bakr, *J. Phys. Chem. Lett.*, 2015, **6**, 3023–3035.
51 X. Sun, X. Tang, Y.-L. Gao, Y. Zhao, Q. Wu, D. Cao and H. Shen, *Nanoscale*, 2023, **15**, 2316–2322.
52 Z.-Y. Wang, M.-Q. Wang, Y.-L. Li, P. Luo, T.-T. Jia, R.-W. Huang, S.-Q. Zang and T. C. Mak, *J. Am. Chem. Soc.*, 2018, **140**, 1069–1076.
53 T. C. Mak and L. Zhao, *Chem. – Asian J.*, 2007, **2**, 456–467.
54 Z. Wang, Y.-M. Sun, Q.-P. Qu, Y.-X. Liang, X.-P. Wang, Q.-Y. Liu, M. Kurmoo, H.-F. Su, C.-H. Tung and D. Sun, *Nanoscale*, 2019, **11**, 10927–10931.
55 M. Zhao, S. Huang, Q. Fu, W. Li, R. Guo, Q. Yao, F. Wang, P. Cui, C. H. Tung and D. Sun, *Angew. Chem., Int. Ed.*, 2020, **59**, 20031–20036.
56 S. Chen, W. Du, C. Qin, D. Liu, L. Tang, Y. Liu, S. Wang and M. Zhu, *Angew. Chem., Int. Ed.*, 2020, **59**, 7542–7547.
57 R. W. Huang, X. Y. Dong, B. J. Yan, X. S. Du, D. H. Wei, S. Q. Zang and T. C. Mak, *Angew. Chem., Int. Ed.*, 2018, **57**, 8560–8566.
58 X.-H. Wu, Z. Wei, B.-J. Yan, R.-W. Huang, Y.-Y. Liu, K. Li, S.-Q. Zang and T. C. Mak, *CCS Chem.*, 2019, **1**, 553–560.
59 P. Chandrashekar, G. Sardar, T. Sengupta, A. C. Reber, P. K. Mondal, D. Kabra, S. N. Khanna, P. Deria and S. Mandal, *Angew. Chem., Int. Ed.*, 2024, **63**, e2023173.
60 Y.-L. Li, W.-M. Zhang, J. Wang, Y. Tian, Z.-Y. Wang, C.-X. Du, S.-Q. Zang and T. C. Mak, *Dalton Trans.*, 2018, **47**, 14884–14888.
61 R. Nakatani, S. Biswas, T. Irie, Y. Niihori, S. Das and Y. Negishi, *ACS Mater. Lett.*, 2023, **6**, 438–445.
62 A. K. Das, S. Biswas, A. Kayal, A. C. Reber, S. Bhandary, D. Chopra, J. Mitra, S. N. Khanna and S. Mandal, *Nano Lett.*, 2023, **23**, 8923–8931.
63 P. Sun, M. Xie, L. M. Zhang, J. X. Liu, J. Wu, D. S. Li, S. F. Yuan, T. Wu and D. Li, *Angew. Chem., Int. Ed.*, 2022, **61**, e202209971.
64 C. Xu, M.-M. Sheng, H.-T. Shi, M. Strømme and Q.-F. Zhang, *Dalton Trans.*, 2019, **48**, 5505–5510.
65 A. K. Das, S. Biswas, A. Thomas, S. Paul, A. S. Nair, B. Pathak, M. S. Singh and S. Mandal, *Mater. Chem. Front.*, 2021, **5**, 8380–8386.
66 Y.-H. Li, R.-W. Huang, P. Luo, M. Cao, H. Xu, S.-Q. Zang and T. C. Mak, *Sci. China: Chem.*, 2019, **62**, 331–335.
67 W.-J. Yen, J.-H. Liao, T.-H. Chiu, Y.-S. Wen and C. Liu, *Inorg. Chem.*, 2024, **63**, 5320–5324.
68 W. A. Dar, A. Jana, K. S. Sugi, G. Paramasivam, M. Bodiuzzaman, E. Khatun, A. Som, A. Mahendranath, A. Chakraborty and T. Pradeep, *Chem. Mater.*, 2022, **34**, 4703–4711.
69 Z.-K. Wang, M.-M. Sheng, S.-S. Qin, H.-T. Shi, M. Strømme, Q.-F. Zhang and C. Xu, *Inorg. Chem.*, 2020, **59**, 2121–2126.
70 C. Xu, N. Hedin, H.-T. Shi and Q.-F. Zhang, *Chem. Commun.*, 2014, **50**, 3710–3712.
71 Z. Wang, X. Y. Li, L. W. Liu, S. Q. Yu, Z. Y. Feng, C. H. Tung and D. Sun, *Chem. – Eur. J.*, 2016, **22**, 6830–6836.
72 K. Zhou, C. Qin, X.-L. Wang, K.-Z. Shao, L.-K. Yan and Z.-M. Su, *CrystEngComm*, 2014, **16**, 7860–7864.
73 Z. Y. Chen, D. Y. Tam, L. L. M. Zhang and T. C. Mak, *Chem. – Asian J.*, 2017, **12**, 2763–2769.
74 X. H. Ma, J. Y. Wang, J. J. Guo, Z. Y. Wang and S. Q. Zang, *Chin. J. Chem.*, 2019, **37**, 1120–1124.
75 X.-Y. Dong, Y. Si, J.-S. Yang, C. Zhang, Z. Han, P. Luo, Z.-Y. Wang, S.-Q. Zang and T. C. Mak, *Nat. Commun.*, 2020, **11**, 3678.
76 S. Das, T. Sekine, H. Mabuchi, S. Hossain, S. Das, S. Aoki, S. Takahashi and Y. Negishi, *Chem. Commun.*, 2023, **59**, 4000–4003.
77 M. Cao, R. Pang, Q.-Y. Wang, Z. Han, Z.-Y. Wang, X.-Y. Dong, S.-F. Li, S.-Q. Zang and T. C. Mak, *J. Am. Chem. Soc.*, 2019, **141**, 14505–14509.
78 M. Cao, S. Wang, J. H. Hu, B. H. Lu, Q. Y. Wang and S. Q. Zang, *Adv. Sci.*, 2022, **9**, 2103721.
79 S.-H. Lu, Y. Li, S.-X. Yang, R.-D. Zhao, Z.-X. Lu, X.-L. Liu, Y. Qin, L.-Y. Zheng and Q.-E. Cao, *Inorg. Chem.*, 2019, **58**, 11793–11800.
80 R. Nakatani, S. Biswas, T. Irie, J. Sakai, D. Hirayama, T. Kawawaki, Y. Niihori, S. Das and Y. Negishi, *Nanoscale*, 2023, **15**, 16299–16306.
81 Z. Wang, Y.-J. Zhu, Y.-Z. Li, G.-L. Zhuang, K.-P. Song, Z.-Y. Gao, J.-M. Dou, M. Kurmoo, C.-H. Tung and D. Sun, *Nat. Commun.*, 2022, **13**, 1802.
82 Z. Wei, X. H. Wu, P. Luo, J. Y. Wang, K. Li and S. Q. Zang, *Chem. – Eur. J.*, 2019, **25**, 2750–2756.
83 Y.-M. Wang, J.-W. Zhang, Q.-Y. Wang, H.-Y. Li, X.-Y. Dong, S. Wang and S.-Q. Zang, *Chem. Commun.*, 2019, **55**, 14677–14680.
84 X.-S. Du, B.-J. Yan, J.-Y. Wang, X.-J. Xi, Z.-Y. Wang and S.-Q. Zang, *Chem. Commun.*, 2018, **54**, 5361–5364.
85 S. Biswas, A. K. Das, A. Nath, S. Paul, M. S. Singh and S. Mandal, *Nanoscale*, 2021, **13**, 17325–17330.
86 J. Sakai, S. Biswas, T. Irie, H. Mabuchi, T. Sekine, Y. Niihori, S. Das and Y. Negishi, *Nanoscale*, 2023, **15**, 12227–12234.
87 Q. Liu and X. Wang, *InfoMat*, 2021, **3**, 854–868.
88 H. T. Ratte, *Environ. Toxicol. Chem.*, 1999, **18**, 89–108.
89 X.-Y. Dong, Y. Si, J.-S. Yang, C. Zhang, Z. Han, P. Luo, Z.-Y. Wang, S.-Q. Zang and T. C. W. Mak, *Nat. Commun.*, 2020, **11**(1), 3678.
90 C.-H. Gong, Z.-B. Sun, M. Cao, X.-M. Luo, J. Wu, Q.-Y. Wang, S.-Q. Zang and T. C. Mak, *Chem. Commun.*, 2022, **58**, 9806–9809.

91 M. Zhang, M. Cao, Z.-B. Sun, Z. Han, Z.-Y. Wang, Q.-Y. Wang and S.-Q. Zang, *Chem. Mater.*, 2023, **35**, 10238–10246.
92 C. Xu, N. Hedin, H.-T. Shi and Q.-F. Zhang, *Chem. Commun.*, 2014, **50**(28), 3710–3712.
93 Z.-K. Wang, M.-M. Sheng, S.-S. Qin, H.-T. Shi, M. Strømme, Q.-F. Zhang and C. Xu, *Inorg. Chem.*, 2020, **59**(4), 2121–2126.
94 M. Zhao, S. Huang, Q. Fu, W. Li, R. Guo, Q. Yao, F. Wang, P. Cui, C.-H. Tung and D. Sun, *Angew. Chem., Int. Ed. Engl.*, 2020, **59**(45), 20031–20036.
95 H. Tang, C. M. Hessel, J. Wang, N. Yang, R. Yu, H. Zhao and D. Wang, *Chem. Soc. Rev.*, 2014, **43**, 4281–4299.
96 A. J. Mannix, B. Kiraly, M. C. Hersam and N. P. Guisinger, *Nat. Rev. Chem.*, 2017, **1**, 0014.
97 H. Liu, Y. Du, Y. Deng and D. Y. Peide, *Chem. Soc. Rev.*, 2015, **44**, 2732–2743.
98 Y. Liu, X. Duan, H.-J. Shin, S. Park, Y. Huang and X. Duan, *Nature*, 2021, **591**, 43–53.
99 V. Adinolfi and E. H. Sargent, *Nature*, 2017, **542**, 324–327.
100 M. Chhowalla, D. Jena and H. Zhang, *Nat. Rev. Mater.*, 2016, **1**, 1–15.
101 M. Galchenko, A. Black, L. Heymann and C. Klinke, *Adv. Mater.*, 2019, **31**, 1900684.
102 F. Fetzer, A. Maier, M. Hodas, O. Geladari, K. Braun, A. J. Meixner, F. Schreiber, A. Schnepf and M. Scheele, *Nat. Commun.*, 2020, **11**, 6188.
103 P. Yuan, R. Zhang, E. Selenius, P. Ruan, Y. Yao, Y. Zhou, S. Malola, H. Häkkinen, B. K. Teo and Y. Cao, *Nat. Commun.*, 2020, **11**, 2229.